In *Tectonic evolution of Asia*, edited by An Yin, and T. M. Harrison, p 208-226, Cambridge University Press, New York, 1996.

11 Diachronous initiation of transtension along the Ailao Shan–Red River shear zone, Yunnan and Vietnam

T. MARK HARRISON, P. H. LELOUP, F. J. RYERSON, PAUL TAPPONNIER, R. LACASSIN, AND CHEN WENJI

Abstract

The Red River shear zone (RRSZ) extends from eastern Tibet to the South China Sea and comprises four elongated massifs. It plays a central role in the hypothesis that strike-slip extrusion of Indochina accommodated a significant portion of the Indo–Asian convergence immediately following the onset of collision. The massifs of the RRSZ contain high-grade metamorphic rocks that were plastically deformed in a left-lateral sense during the mid-Tertiary. $^{40}Ar/^{39}Ar$ analysis of K-feldspars from 10 transects perpendicular to the northwest–southeast strike of the Ailao Shan, the longest massif in the chain, has yielded a pattern of ages consistent with diachronous initiation of transtensional faulting along the RRSZ. The normal component of this faulting occurs along the eastern boundary of the shear zone, the locus of the active Range Front fault. Numerical modeling of isotopically derived cooling histories yields a dip-slip rate of about 6 mm/a. A 400-km-long segment of the Ailao Shan reveals a pattern of ages that increase smoothly from 17 Ma in the northwest Ailao Shan to 25 Ma in Vietnam. This relationship indicates that the onset of extension was diachronous, beginning in the southeast and propagating northwest at a rate of about 4.5 cm/a. This rate and the spatial and temporal variabilities of extension are consistent with prediction, based on Oligocene–early Miocene magnetic anomalies from the South China Sea, that the RRSZ experienced strike-slip rates of 3–5 cm/a and that its present position does not represent a small circle about the Indochina/South China poles of rotation. As a consequence, a strike-perpendicular component of compression would have existed in the northern portion of the belt, with an increasing component of strike-perpendicular extension to the southeast across the Ailao Shan. The general shallowing of foliation from northwest to southeast across the Ailao Shan is consistent with this prediction. Although consistent with predictions of the extrusion hypothesis, the pattern of thermochronology across the Ailao Shan contrasts with a model of rotation of rigid crustal blocks.

Introduction

Identifying and determining the relative importance and temporal variability of the mechanisms responsible for accommodating convergence during the Indo–Asian collision are fundamental to understanding the geologic evolution of Tibet and the Himalaya. For example, it has been firmly established that a portion of the Tertiary convergence was absorbed by intracontinental thrusts in the Lesser Himalaya (e.g., Le Fort, 1986), Tethyan Himalaya (e.g., Burg et al., 1984), and Indus-Tsangpo suture zone (e.g., Yin et al., 1994). While some have speculated that similar amounts of thrust-related thickening occurred throughout Tibet during the Tertiary (e.g., Dewey and Burke, 1973; Dewey et al., 1988), relatively little has been securely documented (Chang et al., 1986). Complicating the simple thickening models is the proposal that continental extrusion accommodated some fraction of the post-50-Ma convergence of India with Eurasia (e.g., Tapponnier et al., 1982, 1986; Peltzer and Tapponnier, 1988; Cobbold and Davy, 1988). Although the two deformational styles are not exclusive of one another, they reflect such disparate views of the response of continental lithosphere to tectonic forces that many researchers attracted to pure thickening models have questioned that predictions of the extrusion hypothesis have been borne out (e.g., England and Houseman, 1986; Dewey, Cande, and Pitman, 1989; England and Molnar, 1990).

Because the Tertiary tectonic evolution of the Red River shear zone (RRSZ) is a key prediction of the hypothesis that extrusion of Indochina accommodated a significant portion of the Indo–Asian convergence (Tapponnier et al., 1982), this feature has been the focus of considerable attention in recent years (e.g., Leloup et al., 1995). Traceable from Tibet through Yunnan to the South China Sea (Figure 11.1), the Red River fault zone had previously been interpreted as either a purely right-lateral fault (e.g., Dewey et al., 1989) or a suture of Proterozoic age (e.g., Fan, 1986; Cheng, 1987), Paleozoic age (e.g., Helmcke, 1985; Wang and Chu, 1988), or Triassic age (e.g., Fan, 1978; Klimetz, 1983; Şengör, 1987; Hutchinson, 1989). According to recent studies, however, the RRSZ is a Tertiary ductile, strike-slip shear zone with a left-lateral offset greater than 80 km (Tapponnier et al., 1990; Schärer et al., 1990; Harrison et al., 1992b; Lacassin, Leloup, and Tapponnier, 1993; Leloup et al., 1993, 1995).

The elongated massifs in Vietnam and Yunnan that define the RRSZ contain metamorphic rocks that have been ductilely

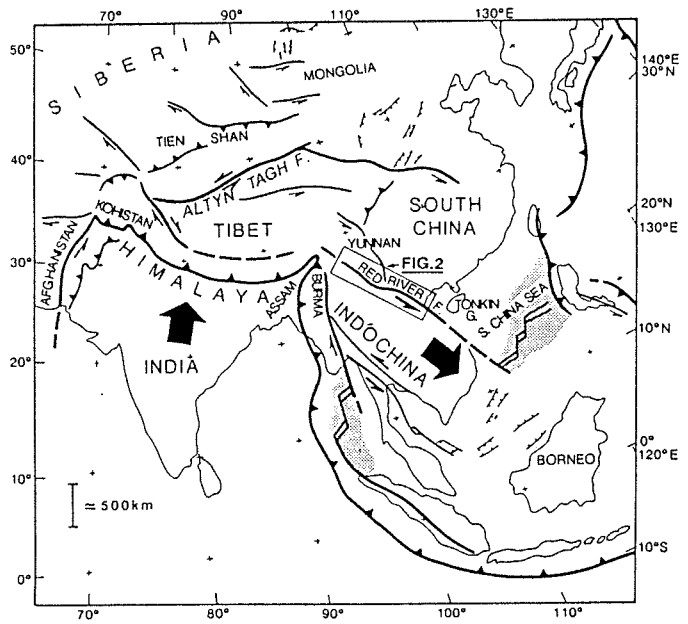

Figure 11.1. Schematic map of the major Cenozoic fault zones in Asia. Tertiary seafloor is shaded. The box shows the location of Figure 11.2. (Adapted from Tapponnier et al., 1982.)

deformed in a left-slip sense. In the continental-extrusion hypothesis, the South China Sea is interpreted to be a pull-apart basin at the southeastern termination of the RRSZ that opened as a result of strike-slip motion (Tapponnier et al., 1982, 1986; Peltzer and Tapponnier, 1988). Magnetic stripes in the South China Sea (Taylor and Hayes, 1980, 1983; Briais, Patriat, and Tapponnier, 1993) are consistent with a left-lateral offset along the RRSZ of about 550 km occurring during seafloor spreading between 32 Ma and about 16 Ma (Briais et al., 1993). This is compatible with a minimum displacement of 330 ± 60 km, estimated from boudinage restoration within the gneiss massifs (Lacassin et al., 1993). The sense of motion on the RRSZ reversed at 5 Ma (Leloup et al., 1993), becoming right-slip, with normal throw in places (Tapponnier and Molnar, 1977; Allen et al., 1984; Leloup et al., 1993).

This chapter presents new $^{40}Ar/^{39}Ar$ findings and stable-isotope results from the RRSZ in Yunnan and Vietnam and summarizes all the available isotope data. These results are then used to constrain models of the thermal and mechanical evolution of the RRSZ. From these models we infer that the RRSZ experienced an increasing component of strike-perpendicular extension toward the southeast. This complex stress history, apparently a consequence of variations in the rotation of Indochina relative to South China, is recorded in the timing of extension-related uplift, which in turn identifies both the polarity and slip rate of the left-lateral shearing event.

Geology of the RRSZ

The RRSZ separates the South China block to the north from the Indochina block to the south (Tapponnier et al., 1990; Leloup et al., 1995). The RRSZ is exposed as a belt of metamorphic massifs ranging from the Xuelong Shan, Diancang Shan, and Ailao Shan in Yunnan to the Day Nui Con Voi in Vietnam (Figure 11.2). These massifs are exposed between Paleozoic to Mesozoic cover rocks and are bounded in many places by Neogene–Quaternary basins (Bureau of Geology and Mineral Resources of Yunnan, 1983). Deformational features in all the metamorphic terranes show consistent evidence of left-lateral shear (Tapponnier et al., 1990; Leloup et al., 1995). Active faults with right-lateral (the Mid-Valley fault) and normal (the Range Front fault) senses of slip bound the (generally) eastern edge of the Ailao Shan (Allen et al., 1984). The western edge of the Ailao Shan massif is defined by the Ailao Shan fault, interpreted to be a northeast-dipping reverse fault (Tapponnier et al., 1990). Active faulting is also present in the Diancang Shan and Day Nui Con Voi ranges in more complex geometries.

The elongated Ailao Shan metamorphic belt (Figure 11.2) offers the longest continuous exposure (~500 km) of the shear zone. In general, northern exposures of the mylonitic gneisses are characterized by steeply dipping foliations in narrow (~10 km) zones of high relief (Figure 11.2). Foliations tend to dip to the northeast in the southern part of the belt, where the shear zone is wider (~20 km) and the topography more subdued. Foliations are steep again in Vietnam, where the southern end of the Ailao Shan bounds the Phan Si Pang granites (Figure 11.2). Foliations are parallel to the strike of the RRSZ throughout the belt, and stretching lineations are generally horizontal (Tapponnier et al., 1990; Leloup et al., 1995) (Figure 11.2, no. 5–14). There is clear evidence of non-coaxial deformation, and kinematic indicators record a left-lateral sense of shear (Tapponnier et al., 1990; Leloup et al., 1993). Ages from syntectonic leucogranitic pods parallel to the foliation and affected by left-lateral shear cluster between 22 Ma and 25 Ma (Schärer et al., 1990, 1994) and are inferred to date late increments of left-lateral shear. Thermobarometric measurements have been interpreted to suggest an elevated geotherm during the left-lateral deformation (Leloup and Kienast, 1993), but could in part reflect a closure phenomenon resulting from rapid denudation (Leloup et al., 1993). $^{40}Ar/^{39}Ar$ results have been interpreted to indicate that ductile left-lateral deformation in the rocks presently outcropping was terminated during the early Miocene, with subsequent oblique unroofing occurring along precursors to a normal fault that presently defines the eastern edge of the massif (Harrison et al., 1992b)

The Diancang Shan (Figure 11.2) is an elongated metamorphic massif (~15 km wide and 80 km long) separated from the Ailao Shan to the south by the Midu Gap, an approximately 80-km segment of brittlely deformed, essentially unmetamorphosed sedimentary rocks (Figure 11.2). The southeastern portion of the Diancang Shan is a horst bounded by two parallel normal faults with opposite dips (Leloup et al., 1993). The northeastern flank exhibits triangularly shaped facets and is bounded by the Er Hai basin, which contains 2,200 m of Quaternary sediment (Guo, Zhang, and Li, 1986). The core of the Diancang Shan consists of high-temperature mylonitic gneisses with a steeply dipping

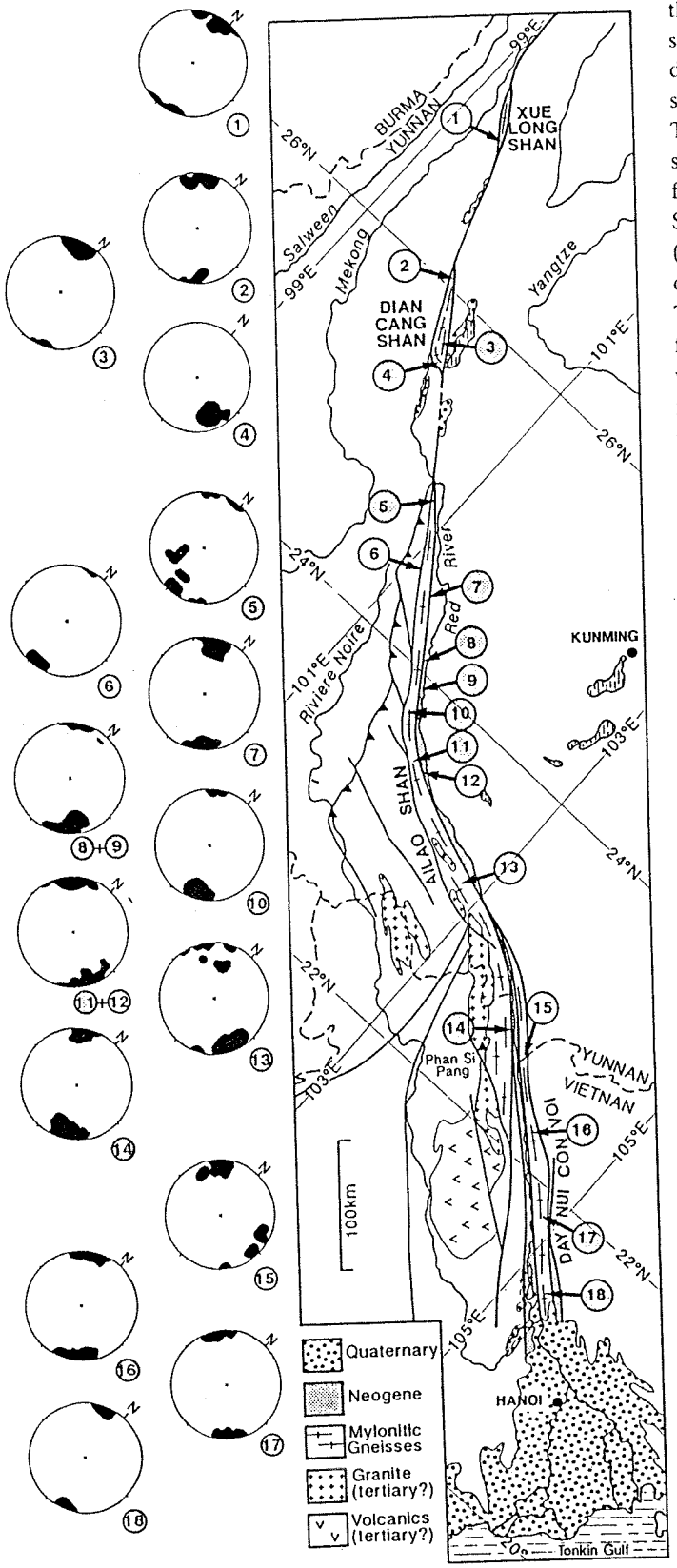

foliation and horizontal stretching lineations (Figure 11.2, no. 3) that show left-lateral shear criteria (Leloup et al., 1993). At the southeastern end of the massif, the high-temperature foliation dips gently to the southeast and contains a stretching lineation slightly oblique to the direction of the belt (Figure 11.2, no. 4). These high-temperature structures are cut by lower-temperature structures (mylonites and fault gouge) indicative of normal faulting along the northeastern flank of the massif. The Diancang Shan is inferred to have experienced two distinct tectonic stages (Leloup et al., 1993). The first was a left-lateral stage of deformation forming high-temperature foliations and lineations. This stage can itself be separated into two successive steps: formation of a simple strike-slip shear zone identical with that visible in the Ailao Shan massif farther to the south, followed by formation of a large left-lateral oblique shear plane affecting the whole shear zone. The direction of movement on this latter shear plane has a vertical component implying uplift of the Diancang Shan massif. This stage is believed to have lasted until about 20 Ma (Leloup et al., 1993; Schärer et al., 1994). The Midu Gap between the Diancang Shan and Ailao Shan massifs is probably due in part to movement along the oblique shear plane. In this interpretation, the Diancang Shan and Ailao Shan massifs represent boudins separated by the Midu Gap (Leloup et al., 1993). Beginning at 4.7 ± 0.1 Ma, the central part of the Diancang Shan shear zone experienced rapid cooling due to uplift of a horst between two presently active normal faults with right-lateral components (Leloup et al., 1993). If that approximately dates the initiation of right-lateral slip in the Ailao Shan, where late Neogene displacement has been estimated by Allen et al. (1984) and Leloup et al. (1995) to have been between 6 km and 40 km, then the average slip rate was between 1 mm/a and 9 mm/a.

The two stages of deformation described earlier (late left-lateral/normal shear plane and active right-lateral/normal faulting) imply differential denudation of the left-lateral shear zone and may explain why the left-lateral deformation is exposed at a higher structural level in the Midu Gap. Active faulting along the

Figure 11.2. Structural map of the RRSZ in the area corresponding to the box outlined in Figure 11.1. Numbers from 1 to 18 indicate the sections where $^{40}Ar/^{39}Ar$ samples (shaded numbers) and structural measurements were taken. Diagrams on the left-hand side are density diagrams of stretching lineations measured in mylonites at each locality (Schmidt projection; lower hemisphere, black areas indicating more than 2% of data concentrated on 1% of hemisphere area). Numbers of structural measurements at each locality: *Xuelong Shan range:* (1) southern end of the Xuelong Shan range (15 measurements). *Diancang Shan range:* (2) northern extremity of the Diancang Shan range (8 measurements); (3) cross section of the Diancang Shan at the latitude of Dali (62 measurements); (4) southern end of the Diancang Shan (24 measurements). *Ailao Shan range:* (5) Wu Ding Shan section (9 measurements); (6) Dongqualing zone (5 measurements); (7) Ejia zone (45 measurements); (8) Gasa section (29 measurements); (9) North Mosha zone (13 measurements); (10) Mosha section (21 measurements); (11) Yuanjiang section (21 measurements); (12) south Yuanjiang section (5 measurements); (13) Yuangang section (16 measurements); (14) Bat Xat section (34 measurements). *Day Nui Con Voi range:* (15) Lao Cay section (8 measurements); (16) Bao Yen section (35 measurements); (17) Yen Binh zone (8 measurements); (18) Baibang site (5 measurements).

Midu Gap (Figure 11.1) is characterized by two different styles: normal faults bounding small basins to the north, and pure right-lateral slip to the south.

About 110 km to the northwest of the Diancang Shan is the Xuelong Shan (Figure 11.2). Observations made at the southern end of this massif (Figure 11.2, no. 1) suggest that it was part of the RRSZ: Most of the rocks are mylonitic; foliation is less steep, but still parallel to the trend of the belt; stretching lineations are horizontal; and many kinematic indicators show a left-lateral sense of shear (Leloup, 1991; Leloup et al., 1995).

The Day Nui Con Voi is the southernmost massif of the RRSZ (Leloup et al., 1995) (Figure 11.2). It runs northwest–southeast for 300 km between the Red River and Song Chay active faults. Toward the southeast, the metamorphic rocks are progressively covered by Quaternary deposits of the Red River delta. Within the massif, most rocks are mylonitic paragneisses, with some mafic and marble boudins. As in the other massifs of the RRSZ, the foliation strikes parallel to the belt. In some areas, especially near Yen Binh and Yen Bai (Figure 11.2, no. 17), foliations are flat-lying. Stretching lineations are always nearly parallel to the belt (Figure 11.2, no. 15–18). Numerous outcrops exhibit criteria consistent with left-lateral shear (Leloup et al., 1995).

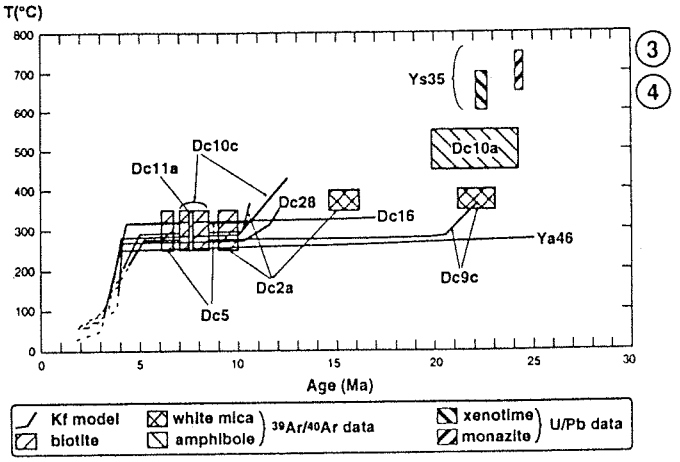

Figure 11.3. Cooling history of the Diancang Shan metamorphic massif. This is Figure 23 of Leloup et al. (1993), augmented by two new results (DC5 and YA46). U-Pb results are from Schärer et al. (1994).

Analytical methods

$^{40}Ar/^{39}Ar$

Mineral separates of K-feldspar, hornblende, biotite, and white mica were obtained using heavy-liquid and magnetic separation techniques from fresh hand specimens. Aliquants of about 15 mg for the K-feldspar and hornblende and about 5 mg for the micas were wrapped in Sn foil and sealed in 6-mm-ID evacuated quartz-glass vials together with Fish Canyon sanidine (FC-3) flux monitors and irradiated in the H-5 position of the Ford Reactor, University of Michigan; see Harrison et al. (1992b) for irradiation details. Aliquants of monitor crystals were individually fused and analyzed for their argon-isotope compositions. J factors were calculated assuming an age of 27.8 Ma for FC-3 (Miller et al., 1985). Analyses of irradiated, vacuum-fused K_2SO_4, CaF_2, and NaCl yielded interfering-neutron-reaction correction factors of $(^{40}Ar/^{39}Ar)_K = 0.026$, $(^{39}Ar/^{37}Ar)_{Ca} = 7.0 \times 10^{-4}$, $(^{36}Ar/^{37}Ar)_{CA} = 2.3 \times 10^{-4}$, and $(^{38}Ar/^{39}Ar)_k = 0.012$.

Samples were either step-heated in a Ta crucible within a double-vacuum furnace or fused using a 5-W Ar-ion laser. Argon blanks over the course of these analyses averaged $2–5 \times 10^{-16}$ mol ^{40}Ar in an atmospheric ratio. $^{40}Ar/^{39}Ar$-isotope measurements were made using VG1200S and VG3600 automated mass spectrometers operated in the electron-multiplier and Daly-detector modes, respectively. A correction for mass discrimination of 0.13%/amu was made to the isotope ratios based on analysis of atmospheric argon. Overall Ar sensitivity for the spectrometers during these analyses typically was $1.0–2.0 \times 10^{-17}$ mol/mV. Further details regarding instrumentation have been given by Harrison et al. (1992b), and routines for peak-height measurements and calculation of associated uncertainties have been given by McDougall and Harrison (1988). A summary of interpreted ages for the biotite, white mica, and hornblende is presented in Table 11.1. K-feldspar-derived thermal histories are shown in Figures 11.3 and 11.4. Age spectra and Arrhenius, $\log(r/r_0)$, and thermal-history plots for two K-feldspar samples (FA-2 and FA-5) are shown in Figures 11.5 and 11.6. Ages were calculated using conventionally accepted decay constants and isotope abundances. Tabulated results of the argon-isotope analyses are available for the cost of reproduction from the first author.

Oxygen/hydrogen isotopes

Whole-rock powders were prepared in a pulverizer and analyzed for oxygen isotopes by conventional fluorination methods (Clayton and Mayeda, 1963) at the University of California, Davis. Results relative to standard mean ocean water (SMOW) are given in Table 11.2. A water sample was analyzed for both O and H isotopes using a MAT 251 mass spectrometer at the University of California, Los Angeles.

Results

$^{40}Ar/^{39}Ar$ thermochronometry

The basis for the closure temperatures used for hornblende, biotite, and white mica has been summarized by McDougall and Harrison (1988). The thermal histories recorded in the K-feldspar $^{40}Ar/^{39}Ar$ age spectra were obtained using a multi-diffusion-domain model (Lovera, Richter, and Harrison, 1989, 1991; Harrison, Lovera, and Heizler, 1991). Two examples of this approach (samples FA-2 and FA-5), shown in detail in Figures 11.5 and 11.6, illustrate the interconnected nature of the age spectrum and the Arrhenius plot and the modeling that

Table 11.1. *Biotite, white mica, and hornblende* $^{40}Ar/^{39}Ar$ results

Sample	Section (number)	Distance along strike (km)	Interpreted age (Ma)	Method
Biotite				
Diancang Shan				
DC10c	Dali (3)	789	7.8 ± 0.7	age spectrum
DC11a	Dali (3)	789	7.6 ± 0.1	isochron
DC2a	South DCS (4)	770	9.5 ± 0.5	age spectrum
DC5	South DCS (4)	770	6.4 ± 0.3	age spectrum
Ailao Shan				
YA24	Wuding Shan (5)	680	24.6 ± 0.4	laser fusion
YU94	Ejia (7)	618	17.8 ± 0.9	isochron
YX29a	Mosha (10)	523	20.7 ± 0.2	isochron
FA-5	Mosha (10)	523	26.4 ± 0.6	isochron
YU38	Yuanjiang (11)	492	22.0 ± 0.5	age spectrum
YU40	Yuanjiang (11)	492	22.8 ± 0.5	age spectrum
FA-8	Yuanyang (13)	396	25.8 ± 0.1	isochron
YU55	Yuanyang (13)	396	26.2 ± 0.5	age spectrum
YU62	Yuanyang (13)	396	22.9 ± 0.2	age spectrum
V103	Bat Xat (14)	273	28.1 ± 0.1	laser fusion
Day Nui Con Voi				
V12	Bao Yen (16)	195	23.1 ± 0.4	laser fusion
V18	Bao Yen (16)	195	23.9 ± 0.2	laser fusion
V20	Bao Yen (16)	196	23.4 ± 0.1	laser fusion
V4	Yen Binh (17)	135	24.9 ± 0.2	laser fusion
V1	Baibang (18)	66	24.1 ± 0.1	laser fusion
White Mica				
DC2a	South DCS (4)	770	15.4 ± 0.8	age spectrum
DC9c	South DCS (4)	770	21.9 ± 0.7	age spectrum
FA-8	Yuanyang (13)	396	29.9 ± 0.1	isochron
Hornblende				
DC10a	Dali (3)	789	22.5 ± 2.0	age spectrum
YU93	Ejia (7)	618	21.6 ± 0.6	isochron
YU97	Ejia (7)	618	20.2 ± 0.2	isochron
YX42b	Gasa (8)	566	22.5 ± 0.4	isochron
FA-2–3	North Mosha (9)	539	21.3 ± 0.7	isochron
YU28	Mosha (10)	523	21.7 ± 0.3	isochron
YX12b	Yuanjiang (11)	492	21.0 ± 1.3	age spectrum
YU56	Yuanyang (13)	396	26.7 ± 0.5	isochron
YU57	Yuanyang (13)	396	23.3 ± 0.4	isochron

permits recovery of the thermal history. The uncertainties in the derived thermal histories usually are ±25°C and ±0.2 m.y. The $^{40}Ar/^{39}Ar$ thermochronologic data were combined with nearby U-Pb ages of monazite (and xenotime) samples where available. Monazite ages are interpreted to date the time of granitoid crystallization (Rapp and Watson, 1986; Rapp, Ryerson, and Miller, 1987; Copeland, Parrish, and Harrison, 1988).

Nearly 70 $^{40}Ar/^{39}Ar$ age spectra were obtained for mineral separates from 43 samples taken from the RRSZ, and 17 of those results have been previously published (Harrison et al., 1992b; Leloup et al., 1993). The samples came from 10 generalized sections along a segment (~700 km) of the belt (Figure 11.2). The position of each section is given in Table 11.1 as the approximate distance along the shear zone from Hanoi. A brief synopsis of the thermal-history results for each section will be given next.

Diancang Shan samples were taken along two east–west cross sections: one at the latitude of Dali (Figure 11.2, no. 3) and one at the southern end of the range (Figure 11.2, no. 4). Two new samples from the Dali section were analyzed. YA46, a K-feldspar from the western part of this section, yielded an age spectrum with apparent ages ranging from 4 Ma to about 23 Ma. That age spectrum was well modeled assuming a nearly isothermal phase at about 270°C (cooling at 1.2°C/m.y. between 25 Ma and 4 Ma), followed by a very rapid cooling beginning abruptly at 4 Ma (Figure 11.3). DC11a biotite from the eastern part of the section yielded an isochron age of 7.6 ± 0.1 Ma, with an initial $^{40}Ar/^{36}Ar$ ratio ($^{40}Ar/^{36}Ar_i$) of 294 (Table 11.1). These

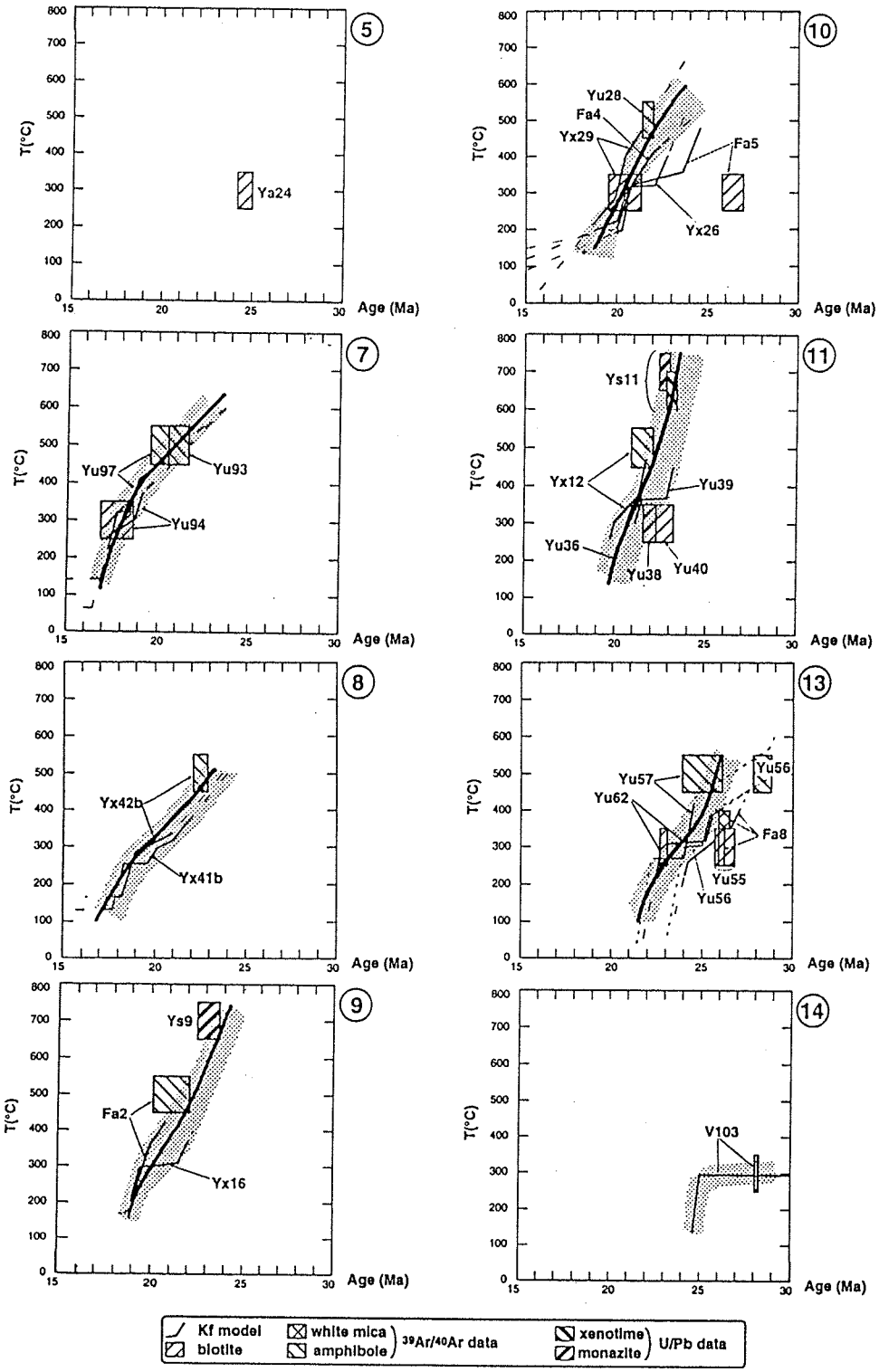

Figure 11.4. Cooling histories along the Ailao Shan range. U-Pb results are from Schärer et al. (1990). Numbers on each diagram are those shown in Figure 11.2. Thick lines correspond to samples located in the central or eastern portions of the massif.

two new results are in agreement with the previously published cooling history for the massif (Leloup et al., 1993).

Ailao Shan samples came from eight sections along the approximately 500-km-long range. From northwest to southeast, we distinguish them as the Wu Ding Shan section (Figure 11.2, no. 5), Ejia zone (Figure 11.2, no. 7), Gasa section (Figure 11.2, no. 8), North Mosha zone (Figure 11.2, no. 9), Mosha section (Figure 11.2, no. 10), Yuanjiang section (Figure 11.2, no. 11), Yuanyang section (Figure 11.2, no. 13), and Bat Xat section (Figure 11.2, no. 14). Thermochronologic results for these sections are shown in Figure 11.4 and will be discussed in turn from northwest to southeast along the strike of the RRSZ.

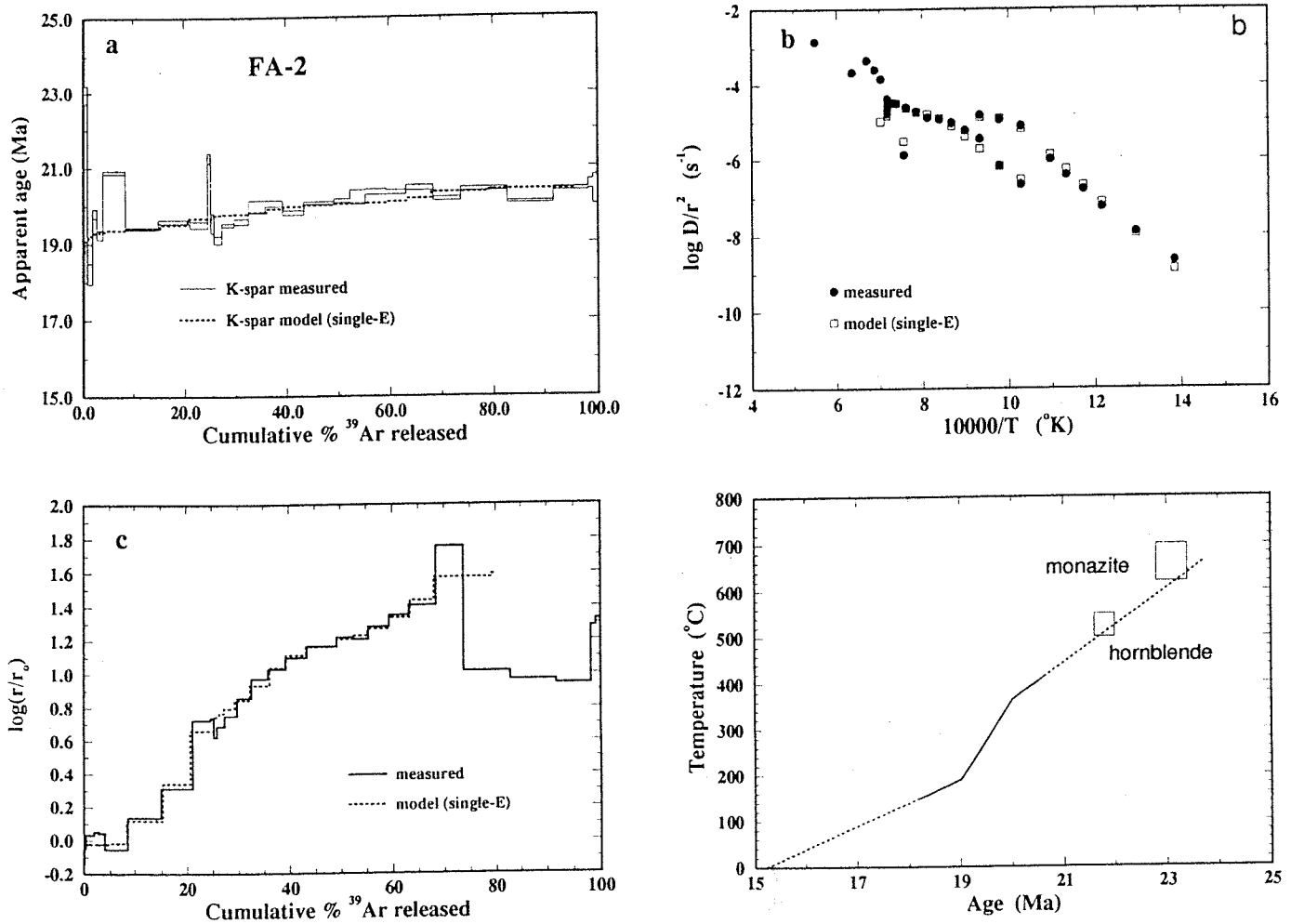

Figure 11.5. FA-2 K-feldspar (a) $^{40}Ar/^{39}Ar$ spectrum and modeled fit, (b) Arrhenius plot calculated from ^{39}Ar diffusivities together with the model fit, (c) $\log(r/r_0)$ plot, and (d) calculated thermal history showing associated hornblende $^{40}Ar/^{39}Ar$ and monazite U-Pb results. The portion of the thermal history constrained by the K-feldspar is shown by the solid line.

1. Wu Ding Shan section (Figures 11.2 and 11.4, no. 5): Biotites from sample YA24 yielded an average laser-total-fusion age of 24.6 ± 0.4 Ma.

2. Ejia zone (Figures 11.2 and 11.4, no. 7): Five minerals from the eastern edge of the Ailao Shan about 80 km south of the Midu Gap were analyzed. Sample YU97 was taken about 10 km northwest of samples YU93 and YU94. Amphiboles from YU97 and YU93 yielded ages of 20.1 ± 0.5 Ma and 20.9 ± 0.8 Ma, respectively. Biotite from YU94 gave an isochron age of 17.8 ± 0.9 Ma ($^{40}Ar/^{39}Ar_i$ = 312). YU97 and YU94 K-feldspars yielded very similar cooling histories, compatible with the ages for the other minerals and indicating rapid cooling from temperatures of about 450°C at about 20 Ma to about 200°C at 17.5 Ma (100°C/m.y., on average). A closer look reveals that both cooling histories contain a slow cooling interval (~1 m.y.) bracketed by two rapid cooling phases, the first starting at 19 Ma at a rate of 170°C/m.y., and the second starting at 17.5 Ma at a rate of 200°C/m.y. Because volume-diffusion information usually is lost due to melting at the temperature at which 80–90% of ^{39}Ar is released, an apparent phase of rapid cooling over the corresponding ages could be a processing artifact, and thus caution in interpretation is advised.

3. Gasa section (Figures 11.2 and 11.4, no. 8): Two samples, YX41c and YX42b, from the eastern edge of the shear zone immediately north of Gasa were analyzed. YX42b amphibole yielded an isochron age of 22.5 ± 0.4 Ma ($^{40}Ar/^{36}Ar_i$ = 309). The thermal histories recovered from K-feldspars YX42b and YX41c suggest cooling from 350°C to 150°C between 21.5 Ma and 18 Ma (~60°C/m.y.). These two thermal histories were truncated by an episode of rapid cooling (>150°C/m.y.). Access to these samples was along a road under construction in 1991, and it is expected that a full west-to-east traverse could now be accomplished.

4. North Mosha zone (Figures 11.2 and 11.4, no. 9): FA-2 amphibole, from an outcrop located 9 km north of Mosha, gave an age of 21.3 ± 0.7 Ma. That age is compatible with the thermal history calculated for the K-feldspar from the same sample, shown in detail in Figure 11.5: cooling from 400°C at 20.5 Ma to 200°C at 19 Ma (130°C/m.y.). This history is consistent with the 23.6 ± 0.6-Ma U-Pb monazite age for sample YS9 located 6 km

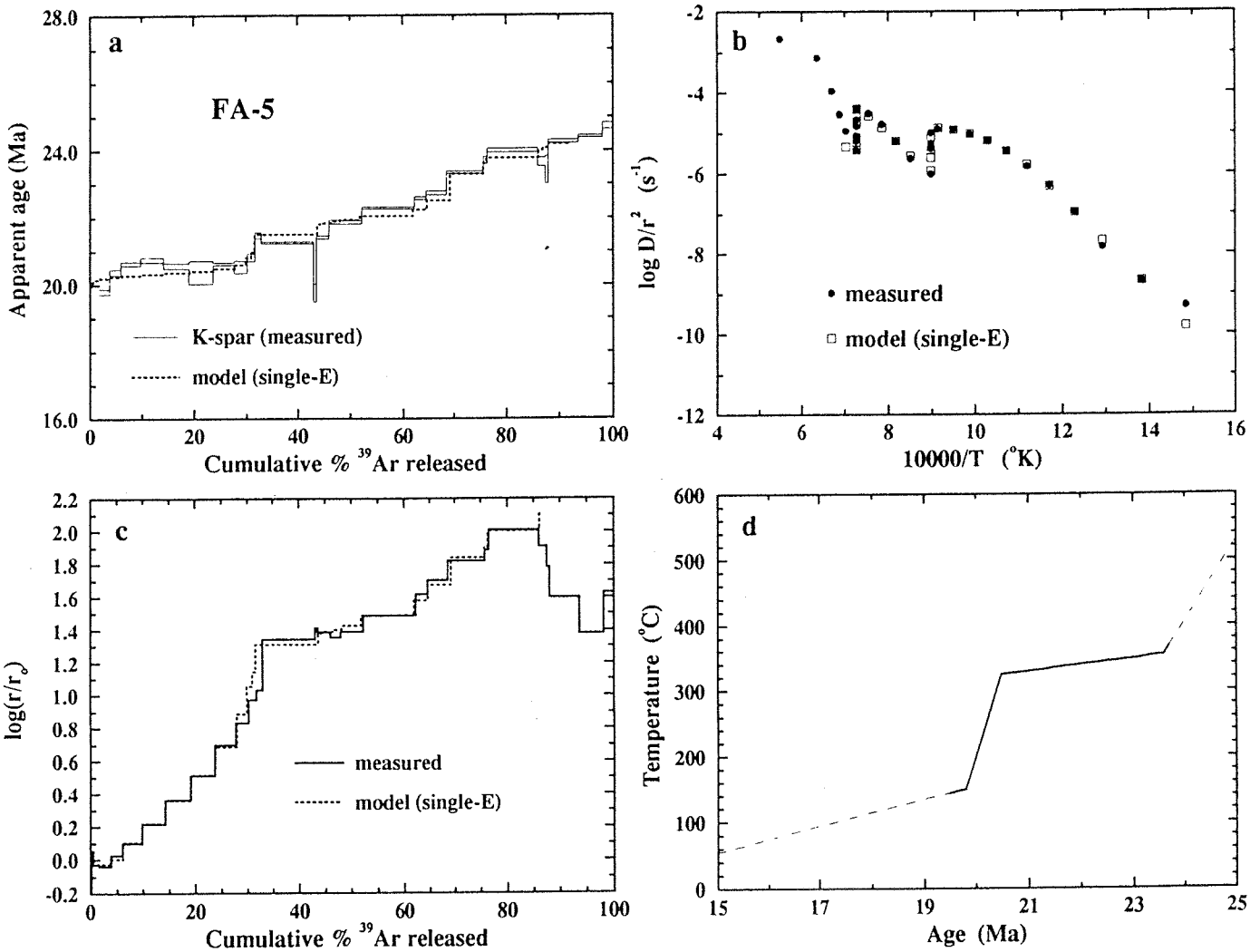

Figure 11.6. FA-5 K-feldspar (a) $^{40}Ar/^{39}Ar$ spectrum and modeled fit, (b) Arrhenius plot calculated from ^{39}Ar diffusivities together with the model fit, (c) log (r/r_0) plot, and (d) calculated thermal history. Note also that the age and closure temperature for the coexisting biotite datum of 26.4 ± 0.6 Ma (Table 11.1) and 350 ± 50°C, respectively, are consistent with the extrapolation of the thermal history constrained by the K-feldspar (shown by the solid line).

farther south (Schärer et al., 1990). K-feldspar YX16, sampled near YS9, showed virtually the same thermal history as FA-2.

5. Mosha section (Figures 11.2 and 11.4, no. 10): Six samples were analyzed across this east–west transect. FA-4 was sampled within several hundred meters of the Range Front fault and 1.25 km from YU28; YX26 and FA-5 came from the southwestern border of the mylonitic gneisses. YX29 was sampled in the middle of the shear zone equidistant between FA-5 and Fa-4. YU28 amphibole gave an isochron age of 21.7 ± 0.3 Ma ($^{40}Ar/^{36}Ar_i$ = 320), and YX29 biotite yielded an age of 20.4 ± 0.9 Ma. The FA-4 temperature history suggests a cooling from 400°C at about 22 Ma to 200°C at about 20 Ma (100°C/m.y.), whereas sample YX29 seems to have reached a similar temperature about 1.5 m.y. earlier (400°C at ~20.5 Ma and 200°C at 18.5 Ma). Note, however, that a number of our samples (including FA-4) were analyzed prior to the recognition that Cl-correlated excess argon can be removed using isothermal duplicate heating steps (Harrison et al., 1994). As a consequence, the thermal history obtained from modeling the uncorrected FA-4 data is probably shifted to older ages by about 1–2 m.y. (Harrison et al., 1992b). FA-5 (Figure 11.6), from the southwest part of the shear zone, showed slow cooling between 23 Ma and 21 Ma, followed by rapid cooling (>150°C/m.y.) starting at 20.8 Ma. The nearby K-feldspar sample YX26 showed a similar cooling history.

6. Yuanjiang section (Figures 11.2 and 11.4, no. 11): YX12 amphibole from the northeastern side of the shear zone yielded an age of 21.5 ± 0.6 Ma, consistent with the cooling history calculated from the coexisting K-feldspar: rapid cooling (>200°C) prior to 21.3 Ma, followed by a phase of cooling at 50°C/m.y. until 20 Ma, when a second phase of rapid cooling started (>200°C). According to the results from YU36 K-feldspar, sampled 2 km farther inside the massif, that second rapid-cooling phase (150°C/

m.y.) began at 21 Ma. Cooling histories for the central part of this section can be inferred from biotite YU38, which gave a 22.0 ± 0.5-Ma age, and YU39 K-feldspar. This K-feldspar indicates a phase of rapid cooling (>150°C/m.y.) following a nearly isothermal period between 22.8 Ma and 21.5 Ma. The cooling histories from the center and northeastern edge of the gneisses are consistent with the U-Pb ages for YS9 monazite and xenotime (22.7 ± 0.3 and 23.1 ± 0.3 Ma, respectively) (Schärer et al., 1990). YU40 biotite, from the southwestern edge of the shear zone, yielded an older age of 22.8 ± 0.5 Ma.

7. Yuanyang section (Figure 11.2, no. 13): This section is unusual in that the dip of the foliation across about three-quarters of the exposure of the shear zone is relatively shallow (~20–30°), with the foliation along the eastern edge of the massif being close to vertical. Ten mineral fractions from this transect were analyzed. As observed in the previous sections, samples from the southwestern part of the shear zone gave older ages than those from the northeast. YU62, from the northeastern edge of the massif, yielded a biotite age of 22.9 ± 0.2 Ma, which agrees with the K-feldspar cooling history, which is itself characterized by very rapid cooling (~200°C/m.y.) interrupted between 25.3 Ma and 22.9 Ma by much slower cooling to just above 300°C. YU57 K-feldspar, located 3.5 km farther south, has a similar cooling history: rapid cooling (280°C/m.y.) until 24 Ma, when very slow cooling intervened at around 220°C until 22.4 Ma, when rapid cooling resumed. Five kilometers farther to the southwest, the thermal history of YU56 K-feldspar has broadly the same shape: cooling at more than 200°C/m.y., interrupted between 25 Ma and 24 Ma by a nearly isothermal phase. YU56 amphibole gave an age of 28.3 ± 0.5 Ma, which is compatible with this cooling history. At the southern border of the gneisses, FA-8 white mica and biotite gave ages of 26.2 ± 0.3 Ma and 26.1 ± 0.2 Ma, respectively, which are similar to that for YU55 biotite (26.2 ± 0.5 Ma). The FA-8 K-feldspar temperature history is in agreement with the micas: rapid cooling (110°C/m.y.) prior to 27 Ma, followed by a slower rate of 10°C/m.y. until 24.3 Ma, when cooling at a rate of 200°C/m.y. began.

8. Bat Xat section (Figures 11.2 and 11.4, no. 14): Along this section, the southernmost of the Ailao Shan, the mylonitic foliation striking northwest–southeast is nearly vertical. Sample V103 came from 7 km within the shear zone. Biotite and K-feldspar $^{40}Ar/^{39}Ar$ ages indicate a simple cooling history: a nearly isothermal phase at 300°C until 25 Ma, when rapid cooling (>300°C/m.y.) began.

Samples from three localities along the Day Nui Con Voi metamorphic massif in Vietnam were analyzed by the $^{40}Ar/^{39}Ar$ method:

1. Bao Yen section (Figure 11.2, no. 14): Four samples from this section, where the structure is similar to that described earlier for the Dali section 600 km farther to the north, were analyzed. All biotite laser-total-fusion ages cluster between 24 Ma and 23 Ma, regardless of position in the section: 23.1 ± 0.4 Ma for V12 from the northeastern side of the massif, and 23.9 ± 0.2 Ma and 23.4 ± 0.1 Ma, respectively, for V18 and V20 from the southwestern side. V12 K-feldspar yielded an age of about 23 Ma for the first 30% of gas release, which then rose abruptly until about 40 Ma. An isochron for the last 57% of ^{39}Ar release gives an age of 40.5 ± 0.7 Ma ($^{40}Ar/^{36}Ar_i$ = 281). This age spectrum suggests that V12 experienced two phases of rapid cooling, as 23 Ma and 40 Ma.

2. Yen Binh zone (Figure 11.2, no. 17): Sixty kilometers farther south, V4 K-feldspar exhibits an age spectrum with a general shape that has been attributed to excess argon (Foster et al., 1990). The apparent ages slowly rise from about 23 Ma during the first 30% of ^{39}Ar release. Between 30% and 70% of release they increase to 29 Ma, before dropping to 27 Ma. The last 35% of gas release corresponds to an age of 27 Ma. An isochron for the last 48% of ^{39}Ar release gives an age of 27.5 ± 0.2 Ma ($^{40}Ar/^{36}Ar_i$ = 290), indicating that this portion of the release was not contaminated. The coexisting laser-total-fusion biotite age is 24.9 ± 0.2 Ma. These results could be interpreted as revealing two phases of rapid cooling at 27.5 M and 23 Ma.

3. Baibang site (Figure 11.2, no. 18): V1 is the southernmost sample from the RRSZ that we analyzed. Its age spectrum has the same shape as that for V4. However, the technical problems encountered during analysis precluded obtaining any detailed quantitative thermal-history information. The coexisting biotite yielded a laser-total-fusion age of 24.1 ± 0.1 Ma.

Oxygen isotopes

To gain a broad picture of volatile migration both during and subsequent to ductile shearing in the Ailao Shan, oxygen-isotope measurements were undertaken on 14 whole-rock samples from the Yuanjiang and Mosha sections (Table 11.2). In general, orthogneisses and paragneisses in the ductile shear zone and meta-sediments west of the Ailao Shan fault have preserved $\delta^{18}O_{SMOW}$ values characteristic of their meta-sedimentary derivation (i.e., 8–13‰) (Faure, 1986). Three samples (YX5b, YX11b, and YX13) yielded lower $\delta^{18}O_{SMOW}$ values of 4.4‰, 5.8‰ and 5.1‰, respectively, likely because of their interaction with meteoric water. As YX5b was sampled only a few meters west of the Ailao Shan fault and YX13 was obtained from within 100 m of the Range Front fault, it appears that the relatively high permeability of those features permitted meteoric fluids to migrate to mid-crustal depths. Although YX11b came from within the ductile shear zone, it was sampled close to an active hot spring, the water from which (YH2O, Table 11.2) plots on the meteoric line (Craig, 1961). Thus the light oxygen may reflect relatively recent exchange with circulating meteoric water. The reconnaissance stable-isotope results from the Ailao Shan tend to support the earlier view of Harrison et al., (1992b) that the gneiss cores and the rocks that encompassed them were not regions of significant hydrothermal activity during the ductile shearing event. Although some evidence does suggest that fluids may have migrated along the bounding faults of the range, penetration within the massif appears not to have been significant.

Oxygen-isotope measurements along two sections through the Diancang Shan yielded findings similar to the Ailao Shan data.

Table 11.2. *Whole-rock oxygen-isotope data*

Ailao Shan		$\delta^{18}O_{SMOW}$ (‰)	δD_{SMOW} (‰)	Location
Yuanjiang section (11)[a]	YX1	13.07		8 km W of AS[b]
YX3c		7.69		3 km W of AS
YX5b		4.44/4.44		10 m W of AS
YX8b		9.04		middle of SZ
YX10		9.48		middle of SZ
YX11b		6.05/5.64		middle of SZ
YX13a		5.11		100 m W of RF
YH20		-10.8/-10.6	-92.7/-92.5	hot-spring water
Mosha section (10)				
YX20		11.31/10.73		6 km W of AS
YX22		13.12		4 km W of AS
YX25b		7.94		50 m E of AS
YX29		8.63		middle of SZ
YU81		8.83		0.5 km W of RF
FA-4		9.46		0.3 km W of RF
Diancang Shan				
South DCS (4)				
DC2a		9.89		7.5 km W of RF
DC3		11.26		7 km W of RF
DC5		8.16		5 km W of RF
DC9c		6.37		4.1 km W of RF
Dali (3)				
DC16		7.14		3.7 km W of RF
DC25c		9.39		2.5 km W of RF
DC28		9.52/9.21		1.4 km W of RF

[a]Section number as indicated in Figure 11.2.
[b]AS, Ailao Shan fault; SZ, shear zone; RF, Range Front fault.

With the exception of DC9c, the only rock analyzed from within a zone affected by a low-temperature deformational fabric, all samples yielded results that are within the range of expected values for the igneous and meta-sedimentary rock types.

Petrography

Rocks of the Xuelong Shan, Diancang Shan, and Ailao Shan massifs are composed of pelitic shales and their high-grade equivalents, amphibolites, biotite-hornblende-bearing orthogneisses, and marbles. The paucity of pelitic rocks makes it difficult to reconstruct the metamorphic field gradient along any section perpendicular to the strike of the shear zone. Nevertheless, it is clear from petrographic evidence that metamorphic grade increases from west to east across the massifs, and by correlating samples along the strike, we can see that the metamorphic field gradient is Barrovian in character.

Essentially unmetamorphosed sediments bound both sides of the Ailao Shan massif. The shear zone itself is bisected parallel to the strike by the Ailao Shan fault, which separates low-grade slates and schists on the southwest side of the massif from gneisses and migmatites on the northeast boundary. The schistose rocks in the southwest are characterized by the assemblage muscovite, chlorite, K-feldspar, and quartz. Metamorphic grade increases to the northeast, reaching biotite grade (the assemblage muscovite, chlorite, biotite, and quartz) in schists immediately adjacent to the Ailao Shan Fault (YX5a, b). Within the Ailao Shan massif, spessartine-rich garnet-bearing pelitic gneisses are found within 1 km of the Ailao Shan fault – sample YU26 from Leloup and Kienast (1993). Gneisses near the fault have been retrogressed to lower-grade assemblages, where retrograde andalusite replaces sillimanite, and chlorite-biotite-muscovite assemblages are developed in pressure shadows around garnet. The rapid increase in metamorphic grade near the Ailao Shan fault is consistent with loss or transposition of section along this feature. Metamorphic grade increases within the gneissic portion of the Ailao Shan massif from sillimanite grade near the Ailao Shan fault to second-sillimanite grade along the northeastern margin, where assemblages of garnet, biotite, sillimanite, and K-feldspar are common, along with migmatites indicative of anatexis. In the Diancang Shan, Leloup et al. (1993) have described staurolite-bearing rocks that are of intermediate grade compared with those of the Ailao Shan schists and gneisses, indicating a shallower structural level.

Various geothermobarometers have been used to quantify

both the metamorphic field gradient and the P–T paths of rocks within the shear zone and along its boundaries. Those results are summarized here and have been reported in more detail by Leloup and Kienast (1993) and Leloup et al. (1993). The vitrinite reflectance of coal from a carbonaceous horizon intercalated with Mesozoic red beds south of Shuangou directly west of section 10 (Figure 11.2) was measured to provide an estimate of the maximum paleo-temperature experienced by the meta-sediments that bound the western side of the massif. The reflectance (R_0) of 4.3 (R. Hill, personal communication) corresponds to a maximum rock temperature of 270–240°C for heating periods between 3 and 30 m.y. (Stach et al., 1982). The temperature at the biotite isograd is poorly constrained, but the first appearance of biotite in Al-poor pelites typically is between 300°C and 400°C (cf. Spear, 1993). The strongly retrogressed pelitic gneisses along the Ailao Shan fault contain relict sillimanite. This constrains the minimum temperature to 470°C (i.e., the Al_2SiO_5 triple point). Leloup and Kienast (1993) also obtained a P–T estimate of about 500°C and less than 3.8 kbar from a retrograde assemblage in one such sample (YU26). These estimates suggest that the temperature discontinuity in the metamorphic field gradient resulting from movement on the Ailao Shan fault is at least 100°C.

Assemblages of garnet, biotite, plagioclase, and sillimanite within the high-grade gneisses of the Ailao Shan massif yield estimates of T = 710 ± 70°C and P = 4.5 ± 1.5 kbar. The temperature estimate is consistent with the granite solidus and the appearance of migmatites along the northern boundary of the shear zone. Hence, the temperature difference recorded in the metamorphic gradient within the gneissic portion of the massif may be as much as 250°C. Because of thermal relaxation of primary-growth zoning in the garnets, P–T-path information could not be obtained from samples in the Ailao Shan. However, a P–T path was obtained from garnet zoning in a staurolite-grade sample from the Diancang Shan (Leloup et al., 1993). The zoning records growth during essentially isothermal decompression at 570°C, starting at about 7 kbar and ending at 5.5 kbar. Assuming that the samples from the Diancang Shan and the Ailao Shan experienced P–T paths of similar character, the retrograde P–T path from Leloup and Kienast (1993) and the garnet growth path from the staurolite-grade sample define a clockwise P–T path (Figure 11.7).

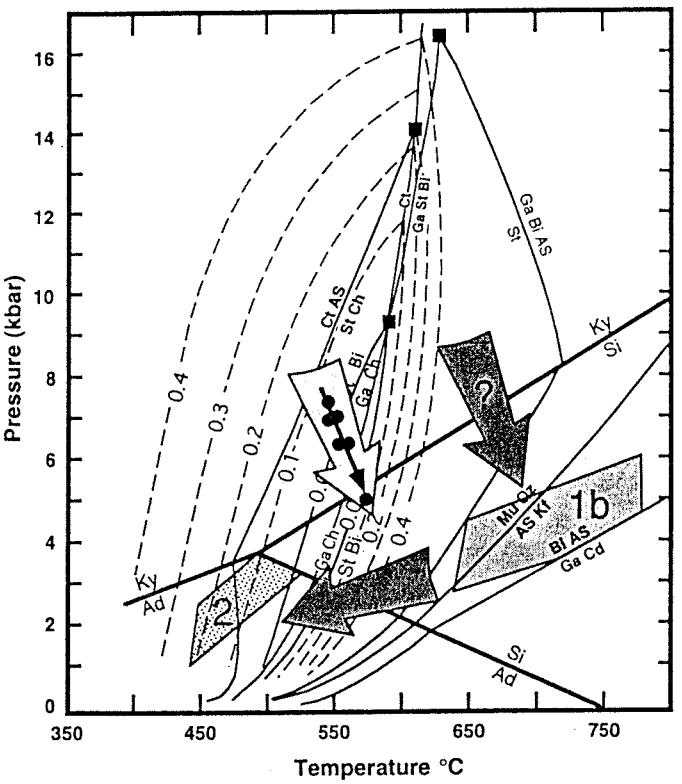

Figure 11.7. Pressure and temperature estimates for the Ailao Shan and Diancang Shan massifs. The estimates are shown on the petrogenetic grid of Spear and Cheney (1989). A P–T path calculated from a zoned garnet coexisting with chlorite and staurolite from within the Diancang Shan, shown by the solid symbols, yields an essentially isothermal decompression path (Leloup et al., 1993). P–T estimates from within the Ailao Shan for rim assemblages containing garnet, biotite, plagioclase, and aluminosilicate are denoted "1b," and a retrograde assemblage is denoted "2" (Leloup and Kienast, 1993). The Ailao Shan data indicate essentially isobaric decompression along the retrograde path. The arrow marked "?" is a possible P–T path for the Ailao Shan samples assuming that they experienced a qualitatively similar history to that of the Diancang Shan.

Thermal modeling

To extract tectonic information from the isotope-derived cooling histories, we have modeled the thermal evolution, following slip on a normal fault, using a finite-difference solution to the generalized equation and the boundary condition

$$\frac{\partial T}{\partial t} = \kappa \nabla^2 T - V \cdot \nabla T + \frac{A_0}{\rho c}$$

$$\hat{n} \cdot \nabla T = -\sigma V$$

on the fault surface, where T is temperature, t is time, κ is the thermal diffusivity, V is slip rate along the fault, A_0 is heat generation, ρ is density, c is heat capacity, σ is flow stress, and $\hat{n}$ is the normal to the fault surface. The numerical scheme utilizes an explicit finite-difference method to obtain the temperature offset resulting from an increment of movement on the fault. This resulting distribution is then relaxed using the alternating-direction implicit method (e.g., Peaceman and Rachford, 1995). The boundary conditions are such that slip on the fault, assumed to occur at an angle of 60°, produces uplift of the footwall block, which is maintained at a constant surface elevation by erosion (Ruppel, Royden, and Hodges, 1988; Harrison et al., 1995a). The fact that footwall cooling first occurs at the greatest distance from the fault, and then progresses toward it (Figure 11.8), restricts the possible angle of slip to more than 45° (Harrison et al., 1995a). The thermal model does not incorporate realistic erosion conditions (i.e., surface topography, variable erosion rates) or syn-tectonic rotation of the fault surface (which we later argue must have occurred). However, these effects are expected to alter the predicted cooling history only when the sample is relatively close to the surface and we restrict our analysis to the

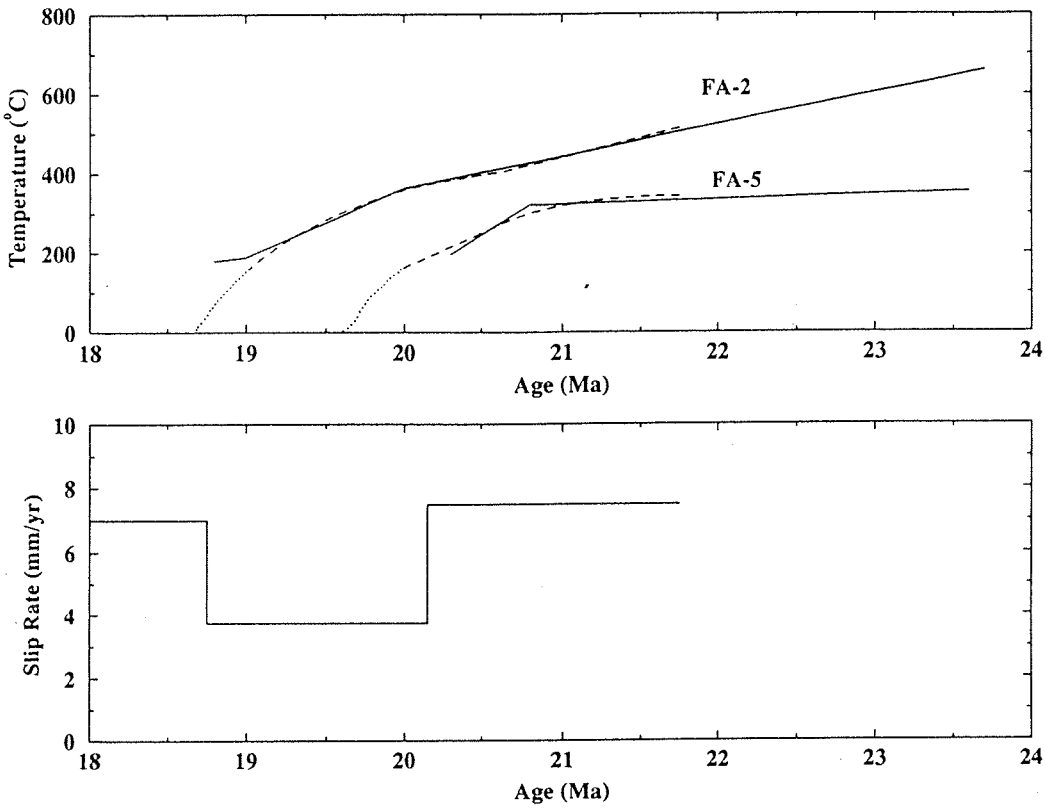

Figure 11.8. (a) Isotope-derived cooling histories from the Mosha transect (FA-5 and FA-2) shown together with calculated results from a finite-difference model of the thermal evolution following slip on a normal fault. The model fit (dashed line) assumes that faulting began at 21.75 Ma, with the slip history shown in (b).

temperature interval 700–200°C. We have focused the thermal modeling on results from the Mosha section, as it is the best-documented of all the traverses, and because of its location in the middle of the Ailao Shan, it contains tectonic elements representative of the massif as a whole.

A variety of constraints of the model can be inferred from the isotope-derived thermal histories, as well as from the petrographic and stable-isotope findings. The oxygen-isotope data (Table 11.2) indicate that neither the Ailao Shan nor the Diancang Shan experienced significant hydrothermal exchange during the high-temperature ductile shearing event, and we thus conclude that heat flow within the core gneisses during that period was predominantly by conduction. We assume, for the purposes of the numerical simulations, the following parameters; $\kappa = 10^{-6}$ m^2/s (Durham, Mirkovich, and Heard, 1987), $A_0 = 10^{-6}$ W/m^3, $\rho = 2{,}850$ kg/m^3, $c = 1{,}000$ J · kg^{-1} · °C^{-1}, and $\sigma = 50$ MPa.

If it is characteristic of the region, the vitrinite reflectance result indicates a peak temperature of about 250°C for the meta-sediments exposed west of the Ailao Shan fault. This temperature estimate is consistent with the petrographic observation that these rocks did not exceed chlorite grade. Bifurcation of the Ailao Shan fault at the latitude of Yuanjiang (Tapponnier et al., 1990, fig. 2C) isolates a sliver a meta-sediment that, in contrast to rocks west of the fault, achieved biotite grade (400–300°C) (Spear, 1993). There is also a marked metamorphic discontinuity between this apparently allocthonous wedge and the retrogressed core gneisses immediately to the east, which, containing sillimanite (Leloup and Kienast, 1993), indicate a temperature greater than 470°C. Because the peak temperature in the thermal reconstruction of FA-5, sampled only a few tens of meters east of the fault, is only about 350°C, peak metamorphic conditions must have occurred prior to the Neogene. For a geotherm of 25–30°C/km (Leloup et al., 1993), the minimum temperature difference across the Ailao Shan fault of about 200°C corresponds to a structural contrast of at least 6 km, implying a thrust sense for this steeply dipping fault.

Assuming that the foliation produced during ductile shearing was vertical prior to the onset of extensional faulting, the present foliation dip angle of about 65°, coupled with the elevation difference between FA-5 and FA-2, implies that they were vertically separated by about 6 km during ductile shearing at 22 Ma. The assumption of initially vertical foliation seems valid, for two reasons. The predicted vertical separation of samples across the shear zone is similar to that obtained independently from thermal-history arguments (see the last paragraph of this section), and the foliation in both the Diancang Shan and northern Ailao Shan, two regions in which we assume little or no early Miocene extension, averages close to vertical. At 22 Ma, the eastern (FA-5) and western (FA-2) boundaries of the Ailao Shan at the latitude of Mosha were at temperatures of 320 ± 25°C and about 450–500°C, respectively (Figure 11.8). The relatively slow cooling recorded by FA-5 between 26 Ma and 21 Ma suggests that this terrane was unlikely to have been far from geothermal equilibrium. For a geotherm of about 25°C/km (Leloup et al., 1993), these temperatures correspond to depths for FA-5 and FA-2 of approximately 12 and 18 km, respectively,

at 22 Ma. The phase of cooling recorded by FA-2 between 24 Ma and 22 Ma may reflect unroofing by another mechanism or the cessation of a transient thermal excursion brought about by injection of anatectic melts (Schärer et al., 1990) high in the section.

Summarizing, the foregoing constraints restrict the principal mode of heat flow during cooling within the massif to conduction, fix the approximate positions of FA-5 and FA-2, both relative to each other and relative to the surface of the earth, at 22 Ma, and indicate the magnitude of the structural discontinuity across the Ailao Shan thrust fault. The only geometric parameter not yet fixed is the distance of FA-2 from the normal-fault surface. Although FA-2 was sampled about 100 m from the presently active Range Front fault, we shall argue later that a progressively greater fraction of the eastern side of the massif has been removed from northwest to southeast. Because of its location in the lesser-affected northern half of the Ailao Shan, a reasonable estimate is that the Mosha section has lost 0.5–2 km.

By iteratively adjusting both the slip-rate history and the timing of initiation of slip, we obtained a good fit to the thermal-history results for both FA-5 and FA–2 (Figure 11.8). In general, the thermal history for FA-5 is the principal control on the timing of fault initiation, whereas the data from FA-2 best constrain the estimate of slip rate. The best-fit forward model was obtained using a relatively simple history: Fault motion began at 21.8 Ma and occurred at a slip rate of 8 mm/a between 21.8 Ma and 20.1 Ma, and at 4 mm/a between 20.1 Ma and 19.0 Ma (Figure 11.8). Changing the distance of FA-2 from the fault from 0.5 km to 2 km does not significantly alter the degree of fit. We find that varying the time of initiation from our preferred value by 0.25 m.y. leads to a mismatch with the empirical cooling history that exceeds our estimate of its accuracy (±25°C and ±0.2 Ma) and thus estimates the apparent onset of faulting at 21.8 ± 0.3 Ma. However, if the fault has a listric geometry, this age could reflect when the presently exposed footwall passed through the brittle–ductile transition and began to move at a high angle.

Despite our simplifying assumptions, there are several conclusions we can draw from these calculations that are insensitive to uncertainties in model parameters. First, there is a thermal lag of about 1 m.y. between the initiation of high-angle faulting and the onset of rapid cooling seen in the K-feldspar thermal histories. For example, although a dramatic increase in the cooling rate for FA-5 occurred at 20.8 Ma, footwall uplift related to extensional faulting began 1 m.y. earlier. Second, the good fit of the model to the empirical results, the high degree of internal consistency of the model framework (e.g., the ~6-km vertical separation of FA-5 and FA-2 is predicted from both geometric and thermal-gradient arguments), and the metamorphic gradient across the Mosha section strongly support the hypothesis that normal faulting was active on the eastern margin of the shear zone simultaneously with strike-slip motion. Finally, the average extension rate calculated for the normal fault at the latitude of Mosha of about 3 mm/a, for the period 22 – 19 Ma, is broadly consistent with that interpolated from Figure 11.12. The misfit of the RRSZ with rotation of the adjacent crustal block at the South China Sea coast suggests an early Miocene extension rate of about 10 mm/a, whereas the value at Ejia is near zero. As Mosha is about one-seventh the distance from Ejia to the South China Sea coast, we thus infer an extension rate there of about 1–2 mm/a. Although broadly consistent, we emphasize that this calculation is subject to considerable uncertainty and is believed to be no more accurate than about a factor of 2.

Tectonic model

On the basis of our earlier and more limited data (Harrison et al., 1992b), we concluded that the Ailao Shan massif was unroofed in a hinged fashion during the early Miocene because of normal faulting along the eastern margin that was contemporaneous with left-lateral slip. Isostatic readjustment following normal slip caused footwall uplift, which in turn led to differential unroofing across the footwall and its subsequent oblique exposure. On both petrologic (increasing metamorphic grade from west to east) and thermochronologic (cooling ages younging from east to west) grounds, we extend this model to the Ailao Shan as a whole, but modify it in one respect by adding diachronism to the onset of extensional faulting along the RRSZ.

The isotope-derived thermal histories for virtually all samples are characterized by a phase of rapid cooling, typically lasting for about 1–2 m.y., that we ascribe to tectonic denudation (Figure 11.4). Because of the nature of argon retention in K-feldspars (Lovera et al., 1989), this cooling episode usually involves the temperature range thought to include the brittle–ductile transition (400–300°C) (Carter and Tsenn, 1987). Thus, at each location we obtain a minimum estimate of the time at which ductile shearing ceased. The most remarkable and, we believe, the most significant feature of the data set is seen in a plot of the times which various isotherms (400°C, 300°C, and 200°C) were achieved as a function of distance along the RRSZ from Hanoi (Figure 11.9). The results show clear correlations, particularly for the two lower and better-constrained temperatures, with slopes that appear to indicate that the brittle–ductile transition migrated through the present exposure of the Ailao Shan from southeast to northwest at a rate of about 4.5 cm/a. The similarity between this figure and the RRSZ slip rate of about 3–5 cm/a estimated by Briais et al. (1993) from South China Sea magnetic anomalies suggests that the trend we observe may reflect processes at the scale of plate tectonics. Although we believe this to be so, the inferred relationship between these two phenomena, involving extensional attenuation of the shear zone, is complex, as reviewed later.

Crustal rocks cool because of erosional denudation, fluid advection, decreasing basal heat flux, lateral heat flow, and tectonic denudation. As we have previously mentioned, the stable-isotope evidence presented herein and the weakly developed nature of retrograde alteration in the Ailao Shan and Diancang Shan (Leloup et al., 1993; Leloup and Kienast, 1993) tend to rule out widespread fluid advection within the massifs. The time scale for cooling due to a decrease in the basal heat input would be substantially longer (tens of millions of years)

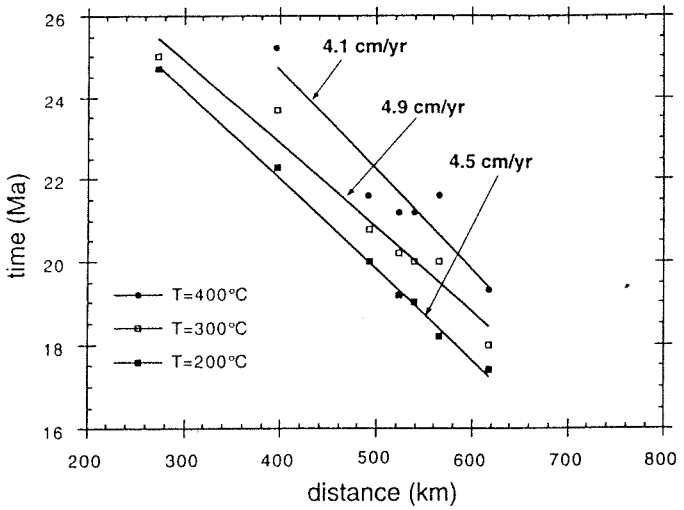

Figure 11.9. Plot of the ages of rapid cooling, as evidenced from K-feldspar-derived thermal histories reaching temperatures of 400, 300, and 200°C, against distance along the strike of the Ailao Shan–RRSZ. The correlation indicates an age–distance relationship of ~4.5 cm/a. It is argued that this is due to the propagation of the brittle–ductile transition from southeast to northwest at a rate corresponding to the strike-slip motion on the RRSZ.

than those observed for cooling of the RRSZ massifs (Figures 11.3 and 11.4). The observed mid-crustal cooling rates, exceeding about 100°C/m.y. require denudation rates that would exceed typical values for surface erosion in moderately thickened crust, but could be accounted for by tectonic denudation. In the preceding section, we quantitatively developed the interpretation that motion on a precursor to the Range Front fault brought cold hanging-wall rock adjacent the footwall, causing it to cool rapidly. Although the thermochronometry in the range of 500–200°C appears to be well described by motion on a high-angle normal fault, it does not explain how samples originally at different depths were brought to the surface together. A mechanical consequence of normal faulting that we have not explicitly modeled, however, may have been responsible for oblique unroofing of the shear zone.

Isostatic rebound following normal faulting tends to both uplift the footwall and rotate the fault surface (Spencer, 1984; Jackson and McKenzie, 1989). When a fault surface is tilted sufficiently far from the optimum angle of slip, the system prefers a new fault to develop in the original orientation (Buck, 1988; Wernicke and Axen, 1988). In that way, rocks on opposite sides of the shear zone that once were separated vertically by several kilometers could reach the present surface together (Figure 11.10a–c). We previously have pointed out (Harrison et al., 1992b) that an additional consequence of this sequence of

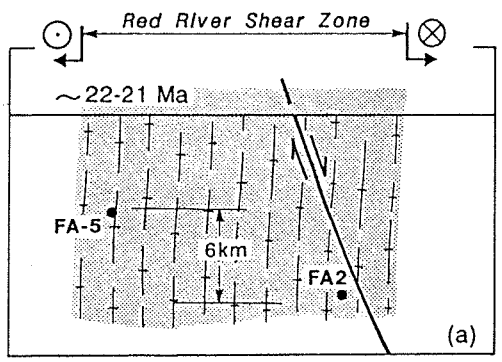

Initiation of normal faulting. Angle of fault based upon assumption of initially vertical foliation.

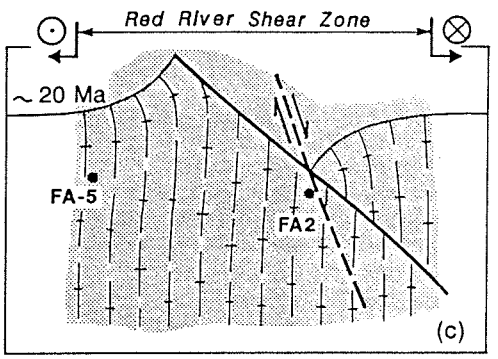

Continued footwall rotation and later initiation of new normal fault in footwall. Places FA–2 apparently closer to fault.

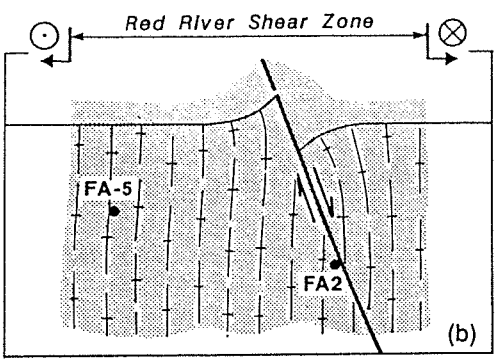

Normal faulting exposes deeper level of eastern Ailao Shan.

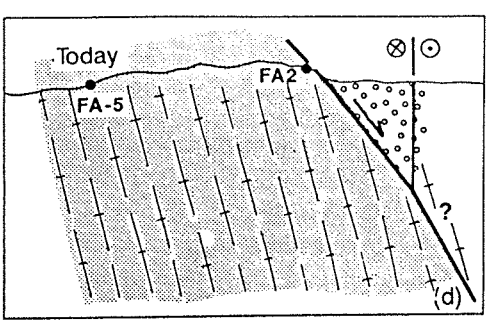

Following denudation.

Figure 11.10. Schematic kinematic model of the Ailao Shan–RRSZ showing the proposed sequence of events that led to differential unroofing. The locations of samples FA-2 and FA-5, originally vertically separated by ~6 km, are shown. (a) A normal fault breaks on the eastern side of the shear zone (paleo-vertical is indicated by stripes); (b) offset occurs along the high-angle fault, with subsequent rotation of the footwall due to isostasy; (c) the footwall experiences further rotation, followed by initiation of a new high-angle normal fault in the footwall; (d) the present-day distribution of samples following denudation. The possible relationship between the Range Front and Mid-Valley faults is shown.

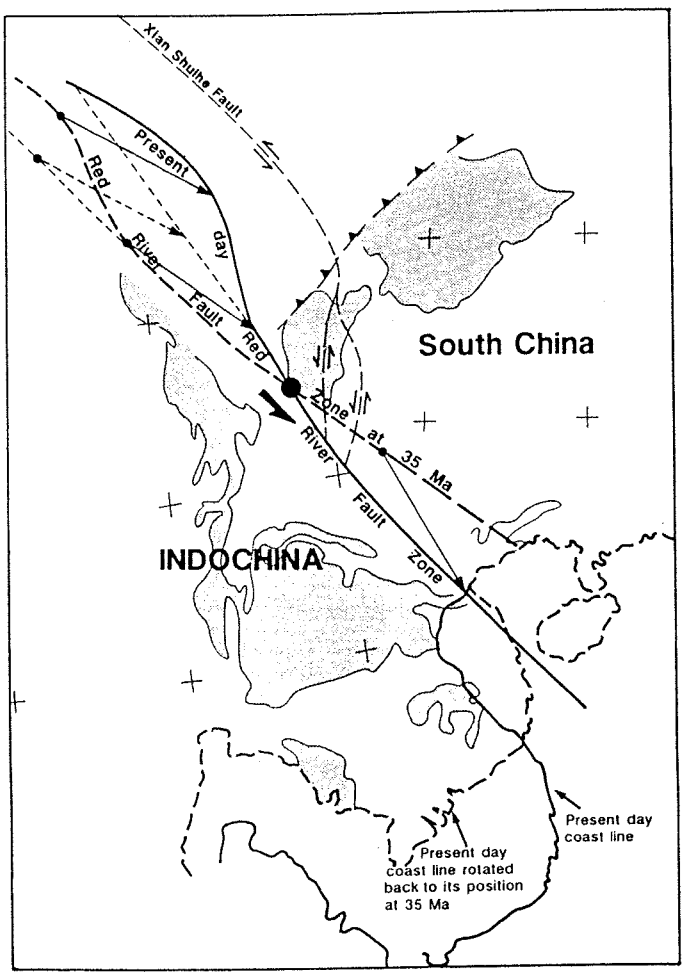

Figure 11.11 Reconstruction of the Ailao Shan–RRSZ at ~35 Ma. The present-day bend of the Ailao Shan was first removed, assuming that it is due to left-lateral motion along the Xian Shuihe fault subsequent to 35 Ma (approximately 100 km of movement). Indochina was then rotated back to its position prior to seafloor spreading in the South China Sea, using the finite pole of rotation of Briais et al. (1993). Gray areas correspond to the Mesozoic red-bed basins of southeast Asia. The large dot designates a zone along the shear zone that did not experience finite extension or compression. All points located along the fault southeast of this large dot experienced finite extension, whereas the ones located to the northwest experienced finite compression. Compression at this point probably was accentuated by its proximity to the Eastern Himalayan syntaxis.

events is episodic removal to the hanging wall of a segment of the footwall each time a new high-angle fault breaks (Figure 11.10c,d). The present exposure of the ductile shear zone would then place a lower bound on its original width, because an unknown portion would have been transferred to the hanging wall. Because the Ailao Shan is directly juxtaposed against low-grade meta-sediments across the Range Front fault (Figure 11.2), material accreted to the hanging wall in this way would subsequently have to be either eroded away or buried.

From the pattern of South China Sea magnetic anomalies, Briais et al. (1993) inferred that the present orientation of the RRSZ is not a small circle about the Indochina/South China poles of rotation (Figure 11.11). Briais et al. (1993) speculated that simultaneously with the Oligocene to early Miocene left-lateral shear, a strike-perpendicular component of compression would have existed north of the present vicinity of the Midu Gap, with a component of strike-perpendicular extension to the southeast of that position. If that were so, then we would predict increasing amounts of extensional strain being recorded in the ductile shear zone southeast across the Ailao Shan. Figure 11.12 shows the deformation rates along the RRSZ predicted from the kinematics of Briais et al. (1993). Whereas the movement is dominantly left-lateral, a component of early Miocene strike-perpendicular extension is predicted between the Midu Gap and the Gulf of Tonkin (Figure 11.1), which would result in progressively greater extensional strain toward the southeast. As mentioned earlier, the integrated rate of extension predicted in the northern Ailao Shan between 25 Ma and 17 Ma of about 2 mm/a is similar to the average extension rate of about 3 mm/a estimated from thermal modeling of normal faulting on the eastern edge of the shear zone (Figure 11.8).

Restating the content of the preceding paragraph, a fixed point relative to the South China Sea spreading center located approximately in the region of the Midu Gap marks the transition from a regime of strike-perpendicular compression to strike-perpendicular extension. Rocks dwelling in the region northwest of this point would experience transpressional stress, while those to the southeast would experience transtensional stress. If crustal extrusion did indeed occur in the fashion proposed by Tapponnier et al. (1982), the movement of rocks through this location should result in a northwestward younging of thermal features associated with extension, the rates of which should be similar to the plate velocities that control this movement. The correlation of thermal history with distance along the fault at the rate predicted by plate kinematics (Figure 11.9) for the early Miocene strongly suggests this relationship.

We earlier argued that normal faulting on the eastern edge of the shear zone would have caused core gneisses of the lower plate to flex upward, inducing differential unroofing of the massif from east to west (Figure 11.10), and that this was consistent with the thermochronologic findings from near Mosha (Figure 11.8). Furthermore, the observation that the foliation in the shear zone varies from essentially vertical in the Diancang Shan and northern Ailao Shan to progressively shallower values toward the southeast indicates that increasing amounts of extensional thinning occurred along the belt. The greater apparent width of the shear zone and the more subdued topography in the southern portion of the range (Leloup et al., 1995) are both consistent with the southern portion of the Ailao Shan having experienced a greater amount of extension relative to the north. As we go farther into Vietnam, we do not see a continuation of the pattern of ages versus distance observed in the Ailao Shan (Talbe 11.1). This is in part expected, as the active fault breaks into two strands in the Day Nui Con Voi, separating this portion of the RRSZ into two massifs (Leloup et al., 1995). Although this structural complexity is not well understood, the "scissorlike" opening of the Hanoi basin that

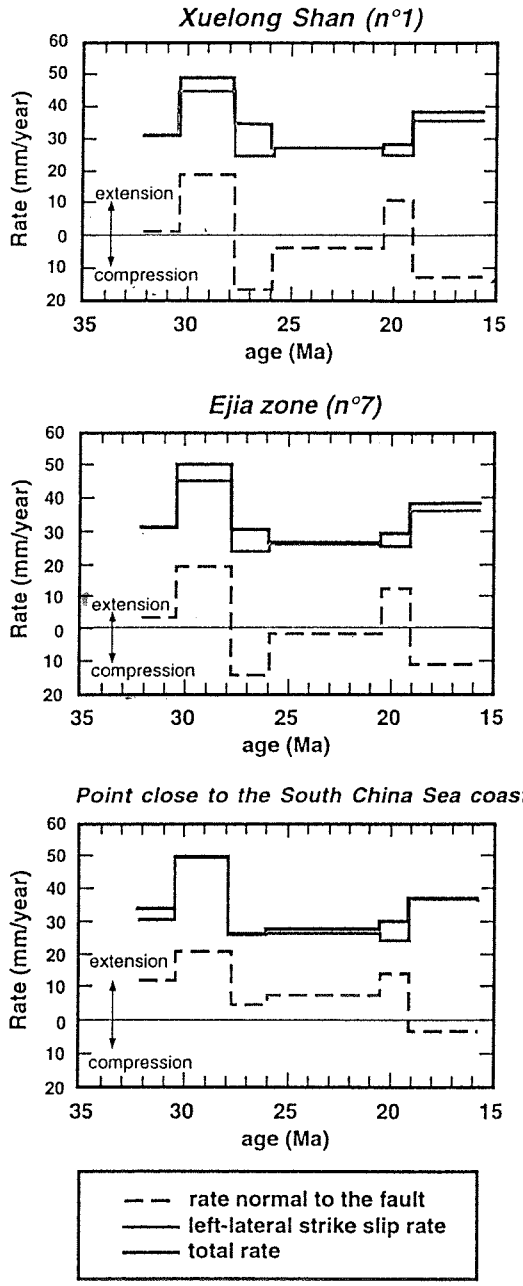

Figure 11.12 Deformation rates along the Ailao Shan–RRSZ deduced from the kinematics of opening of the South China Sea. These rates are calculated for points fixed to the South China block (no movement with respect to their present-day positions). Total rates are from Briais et al. (1993). The strike-slip and strike-perpendicular rates are calculated assuming a 135°N trend for the shear zone. The movement is mostly left-lateral strike slip for all points (~4 cm/a on average), while the component of strike-perpendicular extension increases progressively from northwest (no. 1) to southeast; the point closest to the South China Sea coastline corresponds to point C of Briais et al. (1993).

indents the Gulf of Tonkin is suggestive that transtension occurred along the RRSZ within Vietnam.

A consequence of shear-zone attenuation via extension (Figure 11.10) is that rocks along the eastern edge of the affected shear zone are continually transferred to the hanging wall and lost. Thus, where we can identify differential denudation, and, by implication, extension, we infer that a portion of the ductile shear zone is missing. The greater the amount of crustal thinning, the greater the potential for loss of a portion of the shear zone. This mechanism not only is consistent with our structural, petrologic, and thermochronologic observations but also resolves a paradox implicit in our data – that is, if the shear zone were completely intact, the thermochronologic results, taken at face value, would indicate that the southern part of the Ailao Shan ceased movement at 25 Ma, but that segments progressively farther north could continue deforming ductilely until 17 Ma. Because widespread anatectic pods (Schärer et al., 1990) experienced left-lateral ductile strain at about 23 Ma (Lacassin et al., 1993), strike-slip movement must have continued during at least some of the interval between 23 Ma and 17 Ma. Although it is possible that strain in the southern part of the range between 23 Ma and 17 Ma is localized along brittle faults, evidence for such features is lacking, despite generally good exposures across the numerous east–west transects. The resolution of this paradox appears to be that the shear zone is not completely preserved in the Ailao Shan. As rocks within the shear zone passed through the present position of the Midu Gap, they entered an extensional-stress regime (Figure 11.11), which eventually led to their partial dismemberment. The portion of the shear zone that dwelled longest in the extensional-stress regime (i.e., the region farthest to the southeast) is most likely to have experienced the earliest and greatest amount of attenuation. One implication of this explanation is that ductile deformation, at least between 23 Ma and 17 Ma, was highly localized, perhaps along the eastern edge of the Ailao Shan massif.

The smooth variation in the pattern of ages (Figure 11.9), from 25 Ma in the south (V103) to 17 Ma in the north (YU97), appears to reflect the continuous passage of the shear zone through a fixed point marking the transition between transpressional and transtensional regimes. This point behaves like the coupler in a zipper that is held stationary as the locked teeth are moved into it. Transiting through that point, the teeth are released, and the zipper is opened. Because the manifestation of this effect (Figure 11.9) transited the Ailao Shan at essentially the same rate as that predicted for sinistral strike-slip motion on the RRSZ (Figure 11.12) from opening of the South China Sea (i.e., ~4 cm/a), we conclude that the two features are related to a single process.

When contemplating the foregoing conclusion, one should appreciate that a pivotal element in our interpretation is the K-feldspar thermochronologic results. The continuous nature of the derived thermal histories (Lovera et al., 1989) permits discontinuities in cooling rate to be tightly constrained. Had we relied solely on temperature–time reconstructions based on bulk ages and nominal estimates of their associated closure tempera-

tures, we would not have had the temporal resolution to reveal the cooling-rate changes. Furthermore, as the temperatures recorded by K-feldspars generally span those close to the brittle–ductile transition, they provide a lower age bound on the termination of ductile strike-slip motion within the exposed massifs.

It has been proposed that strike-slip faulting adjacent to the eastern syntaxis of the Indo–Asian collision zone may be due to faults rotating in a clockwise fashion (e.g., Cobbold and Davy, 1988; Dewey et al., 1989; England and Molnar, 1990). However, as depicted by England and Molnar (1990), the model predicts that fault surfaces should have experienced similar stress histories along their entire length. The agreement between the observations presented in this chapter and the extrusion-model prediction of a change in the fault kinematics along the RRSZ between the Diancang Shan and Ailao Shan leads us to conclude that a substantial portion of strike-slip motion on the RRSZ resulted in crustal extrusion to the southeast.

Harrison et al. (1992a) summarized the widespread evidence for an unroofing episode in southern Tibet and the Himalaya during the late Oligocene/early Miocene and linked it to initiation of movement on the Main Central Thrust during the early Miocene, or earlier on the Gangdese thrust. Tapponnier et al. (1986) suggested that major crustal thickening in the Himalaya and Tibet postdated left-lateral motion on the RRSZ and the opening of the South China Sea. Timing constraints suggest that the crustal-scale thrusts in the Himalaya (Harrison, McKeegan, and Le Fort, 1995b) and southern Tibet (Yin et al., 1994) were active during the later phase of left-lateral slip on the RRSZ, suggesting a transition from a dominantly extrusion mode to one in which crustal thickening progressively accommodated a larger fraction of the continuing convergence of India with Asia.

Conclusions

Thermal histories derived largely from $^{40}Ar/^{39}Ar$ analyses of K-feldspars from 10 locations along the RRSZ record a pattern of early Miocene denudation that appears related to transtensional faulting in the southern portion of the belt. Ages progressively increase along a 500-km segment of the Ailao Shan massif from about 17 Ma in the northwest to about 25 Ma within Vietnam. This apparent relationship suggests that the initiation of strike-perpendicular extension along the RRSZ propagated from southeast to northwest at a rate of about 4.5 cm/a. This rate is essentially identical with that predicted along the RRSZ between 27 Ma and 17 Ma from plate-tectonic kinematics. In the Ailao Shan, the normal component associated with transtension is inferred to have occurred along the northeastern boundary of the massif, the site of an active detachment. Numerical modeling of the thermal-history data suggests early Miocene extension rates of about 7% of the sinistral strike-slip rate. This result is broadly consistent with an estimate of the extension rate inferred from the South China Sea magnetic anomalies. Our results indicate that the southern portion of the shear zone experienced a transition from a compressional to tensional stress regime during extrusion, with the rocks farthest to the southeast experiencing the highest extensional strains. They appear inconsistent with a simple model of rotation of rigid blocks. These new results suggest a gradual transition from a dominantly extrusion mode during the Oligocene to a mode in the early Miocene in which crustal thickening in southern Tibet and the Himalaya progressively accommodated a larger fraction of the continuing convergence of India with Asia.

Acknowledgments

This research was supported by grants to T.M.H. (NSF and DOE), F.J.R. (IGPP/LLNL), and C.W. (PRC Seismological Foundation). P.H.L., P.T., and R.L. acknowledge the IPGP DBT program of CNRS/INSU and the Academia Sinica Cooperative Project for support. We thank Matt Heizler and Marty Grove for technical assistance with the argon-isotope analyses, Oscar Lovera for performing the thermal modeling, Bob Criss and Tim Rose for the stable-isotope measurements, and Anne Briais for calculation of slip rates of the RRSZ as deduced from South China Sea magnetic anomalies. We thank An Yin and Peter Cobbold for providing constructive reviews.

References

Allen, C. R., Gillespie, A. R., Han, Y., Sieh, K. E., Zhang, B., and Zhu, C. 1984. Red River and associated faults, Yunnan province, China: Quaternary geology, slip rates, and seismic hazard. *Geol. Soc. Am. Bull.* 95:686–700.

Bence, A. E., and Albee, A. L. 1968. Empirical correction factors for the electron microanalysis of silicates and oxides. *J. Geol.* 76:382–403.

Briais, A., Patriat, P., and Tapponnier, P. 1993. Updated interpretation of magnetic anomalies and seafloor spreading stages in the South China Sea: implications for the Tertiary tectonics of SE Asia. *J. Geophys. Res.* 98:6299–328.

Buck, W. R. 1988. Flexural rotation of normal faults. *Tectonics* 7:959–73.

Bureau of Geology and Mineral Resources of Yunnan. 1983. Geological map of Yunnan, scale 1 : 500,000.

Burg, J. P., Brunel, M., Gapais, D., Chen, G. M., and Lin, G. H. 1984. Deformation of leucogranites of the crystalline Main Central Sheet in southern Tibet (China). *J. Struct. Geol.* 6:535–42.

Carter, N. L., and Tsenn, M. C. 1987. Flow properties of continental lithosphere. *Tectonophysics* 136:27–63.

Chang, C., et al. 1986. Preliminary conclusions of the Royal Society and Academia Sinica 1985 geotraverse of Tibet. *Nature* 323:501–7.

Cheng, Y. 1987. A cognitive basis and discussion on the nappe structure of Ailao Shan–Diancang Shan. *Geol. Yunnan* 6:291–7.

Clayton, R. N., and Mayeda, T. K. 1963. The use of bromine penta-flouride in the extraction of oxygen from oxide and silicates for isotopic analysis. *Geochim. Cosmochim. Acta* 32:415–32.

Cobbold, P. R., and Davy, P. 1988. Indentation tectonics in nature and experiment, 2. Central Asia. *Bull. Geol. Inst. Univ. Uppsala* 14:143–62.

Copeland, P., Parrish, R. R., and Harrison, T. M. 1988. Identification of inherited radiogenic Pb in monazite and its implications for U-Pb systematics. *Nature* 333:760–3.

Craig, H. 1961. Isotopic variations in meteoric waters. *Science* 133:1702–4.

Dewey, J. F., and Burke, K. A. 1973. Tibetan, Variscan and Precambrian basement reactivation: products of continental collision. *J. Geol.* 81:683–92.

Dewey J. F., Cande, S., and Pitman, W. 1989. Tectonic evolution of the India/Eurasia collision zone. *Eclogae Geol. Helv.* 82:717–34.

Dewey, J. F., Shackelton, R. M., Chang C., and Sun, Y. 1988. The tectonic evolution of the Tibetan plateau. *Phil. Trans. R. Soc. Lond.* A327:379–413.

Durham, W. B., Mirkovich, V. V., and Heard, H. C. 1987. Thermal diffusivity of igneous rocks at elevated pressure and temperature. *J. Geophys. Res.* 92:11,615–34.

England, P., and Houseman, G. 1986. Finite strain calculations of continental deformation. 2. Comparison with the India–Asia collision zone. *J. Geophys. Res.* 86:3664–76.

England, P., and Molnar, P. 1990. Right-lateral shear and rotation as the explanation for strike-slip faulting in eastern Tibet. *Nature* 344:140–2.

Fan, C. 1986. The tectonic-metamorphic belt of Mt. Ailao in Yunnan province. *Geol. Yunnan* 5:281–91.

Fan, P. F. 1978. Outline of the tectonic evolution of southwestern China. *Tectonophysics* 45:261–7.

Faure, G. 1986. *Principles of Isotope Geology.*, 2nd ed. New York: Wiley.

Foster, D. A., Harrison, T. M., Copeland, P., and Heizler, M. T. 1990. Effects of excess argon within large diffusion domains of K-feldspar age spectra. *Geochim. Cosmochim. Acta* 54:1699–708.

Guo, S., Zhang, J., and Li, X. 1986. Fault displacement and recurrence intervals of earthquakes on the northern segment of the Honghe river fault zone. *Seismology and Geology* 8:77–89.

Harrison, T. M., Copeland, P., Kidd W. S. F., and Lovera, O. M. 1995a. The Nyainqentanghla shear zone: implications for Tibetan plateau uplift and onset of the Asian monsoon. *Tectonics* 14:658–76.

Harrison, T. M., Copeland, P., Kidd, W. S. F., and Yin, A. 1992a. Raising Tibet. *Science* 255:1663–70.

Harrison, T. M., Heizler, M. T., Lovera, O. M., Chen, W., and Grove, M. 1994. A chlorine disinfectant for excess argon released from K-feldspar during step-heating. *Earth Planet. Sci. Lett.* 123:95–104.

Harrison, T. M., Lovera, O. M., and Heizler, M. T. 1991. $^{40}Ar/^{39}Ar$ results for alkali feldspars containing diffusion domains with differing activation energy. *Geochim. Cosmochim. Acta* 55:1435–48.

Harrison, T. M., McKeegan, K. D., and Le Fort, P. 1995b. Detection of inherited monazite in the Manaslu leucogranite by $^{208}Pb/^{232}Th$ ion microprobe dating: crystallization age and tectonic significance. *Earth Planet. Sci. Lett.*

Harrison, T. M., Wenji, C., Leloup, P. H., Ryerson, F. J., and Tapponnier, P. 1992b. An early Miocene transition in deformation regime within the Red River fault zone, Yunnan, and its significance for Indo–Asian tectonics. *J. Geophys. Res.* 97:7159–82.

Helmcke, D. 1985. The Permo–Triassic "Paleotethys" in mainland Southeast-Asia and adjacent parts of China. *Geol. Rundschau* 74:215–28.

Hutchinson, C. S. 1989. The Paleo-Tethyan realm and Indosinian orogenic system of southeast Asia. In *Tectonic Evolution of the Tethyan Region*, ed. A. M. C. Şengör, pp. 585–643. Orlando, FL: Academic.

Jackson, J., and McKenzie, D. 1989. The geometrical evolution of normal fault systems. *J. Struct. Geol.* 5:471–82.

Klimetz, M. P. 1983. Speculation on the Mesozoic plate tectonic evolution of eastern China. *Tectonics* 2:139–66.

Lacassin, R., Leloup, P. H., and Tapponnier, P. 1993. Bounds on strain in large Tertiary shear-zones of SE Asia from boudinage restoration. *J. Struct. Geol.* 15:677–92.

Le Fort, P. 1986. Metamorphism and magmatism during the Himalayan collision. In *Collision Tectonics*, ed. M. P. Coward and A. C. Ries. *Geol. Soc. London Spec. Pub.* 19:159–72.

Leloup, P. H. 1991. Cinematique des deformations "Himalayennes" dans la zone de cisaillement crustale de l'Ailao Shan-Fleuve Rouge. Thèse de Doctorat, Université Paris 6.

Leloup, P. H., Harrison, T. M., Ryerson, F. J., Wenji, C., Qi, L., Tapponnier, P., and Lacassin, R. 1993. Structural, petrological and thermal evolution of a Tertiary ductile strike-slip shear zone, Diancang Shan (Yunnan, PRC). *J. Geophys. Res.* 98:6715–43.

Leloup, P. H., and Kienast, J.-R. 1993. High temperature metamorphism in a major strike-slip shear zone: the Ailao Shan–Red River, P.R.C. *Earth Planet. Sci. Lett.* 188:213–34.

Leloup, P. H., Lacassin, R., Tapponnier, P., Schärer, U., Zhong, D., Lui, X., Zhang, L., Ji, S. and Phan T. T. 1995. The Ailao Shan–Red River shear zone (Yunnan, China), Tertiary transform boundary of Indochina. *Tectonophysics* 251:3–84.

Lovera, O. M., Richter, F. M., and Harrison, T. M. 1989. $^{40}Ar/^{39}Ar$ geothermometry for slowly cooled samples having a distribution of diffusion domain sizes. *J. Geophys. Res.* 94:17,917–35.

Lovera, O. M., Richter, F. M., and Harrison, T. M. 1991. Diffusion domains determined by ^{39}Ar release during step-heating. *J. Geophys. Res.* 96:2057–69.

Lyon-Caen, H., and Molnar, P. 1983. Constraints on the structure of the Himalaya from an analysis of gravity anomalies and a flexural model of the lithosphere. *J. Geophys. Res.* 88:8171–92.

McDougall, I., and Harrison, T. M. 1988. *Geochronology and Thermochronology by the $^{40}Ar/^{39}Ar$ Method.* Oxford University Press.

Miller, D. S., Duddy, I. R., Green, P. F., Hurford, A. J., and Naeser, C. W. 1985. Results of interlaboratory comparison of fission-track age standards: fission-track workshop, 1984. *Nucl. Tracks* 10:383–91.

Peaceman, D. W., and Rachford, H. H. 1955. The numerical solution of parabolic and elliptic equations. *J. Soc. Indust. Appl. Math.* 3:28–41.

Peltzer, G., and Tapponnier, P. 1988. Formation and evolution of strike-slip faults, rifts, and basins during the India–Asia collision: an experimental approach. *J. Geophys. Res.* 93:15,085–117.

Rapp, R. P., Ryerson, F. J., and Miller C. F. 1987. Experimental evidence bearing on the stability of monazite during crustal anatexis. *Geophys. Res. Lett.* 14:307–10.

Rapp, R. P., and Watson, E. B. 1986. Monazite solubility and dissolution kinetics: implications for thorium and light rare earth chemistry of felsic magmas. *Contrib. Mineral. Petrol.* 94:304–16.

Richter, F. M., Lovera. O. M., Harrison, T. M., and Copeland, P. C. 1991. Tibetan tectonics from $^{40}Ar/^{39}Ar$ analysis of a single K-feldspar sample. *Earth Planet. Sci. Lett.* 105:266–76.

Ruppel, C., Royden, L., and Hodges, K. V. 1988. Thermal modeling of extentional tectonics: application to pressure-temperature-time histories of metamorphic rocks. *Tectonics* 7:947–57.

Schärer, U., Tapponnier, P., Lacassin, R., Leloup, P. H., Zhong, D., and Ji, S. 1990. Intraplate tectonics in Asia: a precise age for large-scale Miocene movement along the Ailao Shan–Red River shear zone, China. *Earth Planet, Sci. Lett.* 97:65–77.

Schärer, U., Zhang, D., and Tapponnier, P. 1994. Duration of strike-slip movements in large shear zones: the Red River belt, China. *Earth Planet. Sci. Lett.* 126:379–97.

Şengör, A. M. C. 1987. Tectonic subdivisions and evolution of Asia. *Bull. Tech. Univ. Istanbul* 40:355–438.

Spear, F. S. 1993. *Metamorphic Phase Equilibria and Pressure-Temperature-Time Paths.* Washington, D.C.: Mineralogical Society of America.

Spear, F. S., and Cheney, J. T. 1989. A petrogenetic grid for pelitic schists in the system SiO_2-Al_2O_3-FeO-MgO-K_2O-H_2O. *Contrib. Mineral. Petrol.* 101:149–64.

Spencer, J. E. 1984. Role of tectonic denudation in warping and uplift of low-angle normal faults. *Geology* 12:95–8.

Stach, D., Mackowsky, M.-T., Teichmuller, M., Taylor, G. H., Chandra, D., and Teichmuller, R. 1982. *Stach's Textbook of Coal Petrology,* trans. D. G. Murchison, G. H. Taylor, and F. Zierke. Stuttgart: Gebrüder Borntraeger.

Tapponnier, P., and Molnar, P. J. 1977. Active faulting and tectonics of China. *J. Geophys. Res.* 82:2905–30.

Tapponnier, P., Lacassin, R., Leloup, P. H., Schärer, U., Zhong, D., Ji, S., Wu, H., Zhong, J., Zhang, L., and Liu, X. 1990. The Ailao Shan/Red River metamorphic belt: Tertiary left-lateral shear between Indochina and South China. *Nature* 343:431–7.

Tapponnier, P., Peltzer, G., and Armijo, R. 1986. On the mechanics of the collision between India and Asia. In *Collision Tectonics,* ed. M. P. Coward and A. C. Ries. *Geol. Soc. London Spec. Pub.* 19:115–57.

Tapponnier, P., Peltzer, G., Le Dain, A. Y., Armijo, R., and Cobbold, P. 1982. Propogating extrusion tectonics in Asia: new insights from simple experiments with plasticine. *Geology* 10:611–16.

Taylor, B., and Hayes, D. E. 1980. The tectonic evolution of the South China Basin. In *The Tectonic and Geologic Evolution of Southeast Asian Seas and Islands,* ed. D. E. Hayes, pp. 23–56. Washington, DC: American Geophysical Union.

Taylor, B., and Hayes, D. E. 1983. Origin and history of the South China Basin. In *The Tectonic and Geologic Evolution of Southeast Asian Seas and Islands, Part 2,* ed. D. E. Hayes, pp. 9–104. Washington, DC: American Geophysical Union.

Wang, E., and Chu, J. J. 1988. Collision tectonics in the Cenozoic orogenic zone bordering China, India and Burma. *Tectonophysics* 147:71–84.

Wernicke, B., and Axen, G. J. 1988. On the role of isostasy in the evolution of normal fault systems. *Geology* 16:848–51.

Yin, A., Harrison, T. M., Ryerson, R. J., Chen, W., Kidd, W. S. F,. and Copeland, P. 1994. Tertiary structural evolution of the Gangdese thrust system, southeastern Tibet. *J. Geophys. Res.* 99:18,175–201.